Additive Manufacturing 82 (2024) 104023

Contents lists available at ScienceDirect

Additive Manufacturing

journal homepage: www.elsevier.com/locate/addma

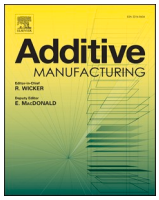

On the thermal emissive behavior of four common alloys processed via powder bed fusion additive manufacturing

César A. Terrazas-Nájera [a,b], Alfonso Fernández [a,b], Ralph Felice [c], Ryan Wicker [a,b,*]

[a] W. M. Keck Center for 3D Innovation, The University of Texas at El Paso, El Paso, TX 79968, USA
[b] Department of Aerospace and Mechanical Engineering, The University of Texas at El Paso, El Paso, TX 79968, USA
[c] FAR Associates, Macedonia, OH 44056, USA

ARTICLE INFO

Keywords:
Emissivity
Solidification
Multi-wavelength pyrometry in PBF AM
Phase changes
Radiation thermometry and thermal monitoring

ABSTRACT

Current thermal monitoring methods used in metal powder bed fusion (PBF) additive manufacturing (AM) rely on a priori knowledge of the emissivity, which is usually assumed temperature, wavelength, and time invariant. Given the true dynamic nature of emissivity for a given material, these assumptions result in the calculation of inaccurate process temperatures, or in the reporting of radiant intensity or radiance temperature as a proxy for the absolute temperature. In this work, we detail the use of a multi-wavelength (MW) pyrometry technique, operating in the spectral range from approximately 900–1700 nm, to capture radiant intensity emissions during processing of various materials using the electron-beam powder bed fusion (PBF-EB) process. The technique measured spectral intensity and analyzed the results of these data after processing with Planck's distribution law in its two-color or ratio pyrometry form to establish the spectral and temporal emissive behavior in the active range from 1080–1637 nm. Four commonly used alloys (Ti6Al4V, TiAl, 316 L, and IN625) were examined here as each of these alloys underwent transitions (from powder to liquid to structured solid) induced during processing. For each material studied, analysis of the aggregated data for ten layers, superimposed in time, identified specific and repeatable trends in the emissivity, with plotted measurements forming clusters or regions in each of the processing stages (preheating, melt scanning, liquid, and cooldown). Also, the data recorded by the MW pyrometer was used to analyze the spectral variability of measurements as well as temporal changes in emissive behavior (from gray to non-gray) at similar temperatures and points in time in each processing stage but during different layers or scans. The results show that the measured emissive behaviors for the four materials were highly variable during processing, with typical differences during transitions ranging from 20% to 75%, and as high as 300% for the case of Ti6Al4V, indicating emissive behaviors that are highly dynamic rather than temporally and spectrally invariant. This dynamic emissive behavior is associated with changes in temperature, morphology, phase, and chemistry of the processed metal that happen during the highly transient and non-equilibrium conditions of PBF AM, and that can only be accounted for by performing in situ measurements during processing using techniques that do not rely on prior knowledge of the emissivity. These results are intended to (1) better inform the additive manufacturing community on the physical nature of emissivity of metallic materials during processing, and (2) provide foundational emissivity data that can be used to improve numerical modeling and the application of radiation thermometry techniques in PBF AM. Further, these results indicate that the emissive behavior during processing can result in significant variations temporally and spectrally, and although the results can be used as foundational emissive behavior measurements, the authors recommend the use of in situ techniques that operate without prior knowledge of emissivity to reduce uncertainties in measurements during PBF AM.

1. Introduction

Significant advances over the last few decades have led to the maturation of powder bed fusion (PBF) metal additive manufacturing (AM) for various applications in highly regulated industries. This has required the in situ monitoring of process signatures to ensure stability

* Corresponding author at: W. M. Keck Center for 3D Innovation, The University of Texas at El Paso, El Paso, TX 79968, USA.
E-mail address: rwicker@utep.edu (R. Wicker).

https://doi.org/10.1016/j.addma.2024.104023
Received 15 September 2023; Received in revised form 29 January 2024; Accepted 1 February 2024
Available online 5 February 2024

and quality using a variety of sensors [1–5]. Process temperature is arguably the most important signature to be monitored for it relates the thermo-mechanical history during processing with the resulting properties and performance of produced components, as indicated by the process-structure-property-performance (PSPP) paradigm. Recently, thermal monitoring of PBF processing has been an intensive research focus. However, techniques commonly employed for monitoring of thermal signatures usually rely on a priori knowledge of the emissivity for measured targets which is also most often assumed to be temporally, thermally and spectrally constant (i.e. graybody behavior) over the spectrum of the sensor employed to carry out measurements [6]. This has been the case for a variety of radiation thermometers used for monitoring at various length scales in PBF AM, including imaging and single spot sensors operating in the visible and infrared (IR) spectral ranges, using techniques such as brightness, ratio, or multi-wavelength pyrometry [7–19]. However, inspection of the largest compilation of the behavior of emissivity and reflectance, the TPRC Data Series [20], shows a significant spectral dependence of these parameters for metals and alloys. The data reported in the referenced work is for material samples carefully prepared and in a stable state. The samples vary in chemistry, temperature, and preparation, and show significant differences in the optical parameters correlating with these variations.

Although the graybody assumption is often applied for radiation thermometry in metal PBF, this assumption is generally unwarranted as is demonstrated generally for metals in the TPRC [20] and confirmed in this work for four specific PBF metallic materials. In reality, the emissive behavior for a given target is highly dynamic, exhibiting variability due to the target's characteristics including its temperature, physical phase, surface morphology, and chemistry [20,21]. Additionally, complications in measurements can arise due to sensor waveband, experimental technique, environmental absorption, and even temporal variability for a given sample. Further, the experimental and calibration methods employed are also often invasive, and thus, may alter the in process thermal conditions for which they are attempting to measure.

The spectral and temporal variability of the emissive behavior for the material being observed during many processes, including PBF AM, is often not considered during the application of thermal radiation measurement techniques. Under the rapidly changing conditions seen in PBF AM, materials experience changes in temperature, phase, surface morphology, and chemistry, all of which contribute to variations in emissivity. Further, as has been shown previously [22] as well as in the following, additional complications arise due to spectral variations in emissivity and even varying spectral behavior during repeated processing. All of these are factors and variability that can lead to highly uncertain temperature measurements. As a result, accurate thermal signatures might only be realized from in situ measurements using radiation thermometry techniques that are not subjected to prior knowledge of emissivity.

In this work, we report on the use of a multi-wavelength (MW) pyrometry technique [23,24] to measure the in-process thermal emissions (absolute temperatures and spectral emissivity) during electron beam powder bed fusion (PBF-EB) processing of four commonly employed metal alloys; Ti6Al4V, TiAl, 316 L, and IN625. Our group demonstrated this technique previously using copper and IN625, showing the ability to measure absolute temperatures and spectral emissivity while also using it as an advanced in situ process diagnostic tool to capture process anomalies [22,25]. While the MW pyrometer employed in this work was originally designed and its accuracy demonstrated for more benign and rather constant processes including induction-heated vacuum investment casting [26,27], its application in this work demonstrated its effectiveness at capturing data in regions of interest for the highly transient process of powder bed fusion. The current research employed this MW pyrometry technique to capture process emissions during PBF-EB processing of four common materials, revealing, for the first time, specific spectral details of the complex and dynamic emissive behavior of these materials while undergoing transformations from powder to liquid to solid. The dynamic thermal emissive behaviors measured for these four materials improve understanding of the physical behavior of emissivity during processing and reveal the potential limitations imposed on the accuracy of measurements made through commonly used emissivity dependent imaging and single spot radiation thermometry techniques. This work highlights the need to employ emissivity independent, and in situ sensing radiation thermometry in PBF should the goal be to attain accuracy in thermal measurements. The following describes the technique and experiments performed that demonstrate the spectral dependence and transient behavior of emissivity as a function of temperature, phase, surface morphology, and chemistry in the measurement system's active range of 1080–1637 nm. It is intended that the data presented in and provided through this work will benefit the AM community in the development of thermal monitoring techniques of increased accuracy while also supporting the development of physics informed and improved numerical models used to simulate PBF processes.

2. Materials and methods

2.1. Metal alloys

The alloys evaluated in this study were Ti6Al4V, gamma titanium-aluminide (TiAl), stainless steel 316 L and Inconel 625 (IN625). Fig. 1 shows scanning electron microscopy (SEM) images for the stock powders taken on a JEOL IT500LV (Tokyo, Japan) microscope. The particle size distribution properties of the feedstocks are listed in Table 1 and the chemistry in Table 2 as per vendor information. The powder production methods were vacuum induction melt argon gas atomization for TiAl, advanced plasma atomization for Ti6Al4V, and argon gas atomization for both 316 L and IN625.

2.2. Experimental setup and instrumentation

Sufficient self-contained detail of the experimental setup is provided here, although specifics of the setup, including schematics detailing the experimental apparatus, are provided in [25]. Briefly, the experimental setup included installation of a multi-wavelength (MW) pyrometer into two commercial PBF-EB systems using a custom developed vacuum rated fixture to allow for near-continuous measurements (images of the experimental setups are provided in Fig. 3 with associated discussion in Section 2.5). The vacuum rated fixture consisted of two KF40 tubes (providing a total length of 450 mm) connected by flanges and vacuum clamps to a custom machined stainless-steel interface that is fitted in the available port atop the chamber of the PBF-EB systems. At the opposite end of the vacuum rated extension tube, a 6 mm thick quartz GE 124 glass (QSI Quartz Scientific, OH, USA) was bonded with vacuum rated cement. Following the quartz glass, the end optic was attached, and the coupling fiber connected to it to transmit the intensity of the target into the FMPI. The entire optical path assembly provided a total focal length of 762 mm resulting in a target spot size with a diameter of ~2.7 mm. It should be noted that the measurement setup (PBF-EB system) and device (FMPI MW pyrometer) used here and described previously [22,25] enable the unique insight into the emissive behavior of these materials during PBF processing by ensuring the optical path remains unobstructed by metallization originating from metal vaporization and condensation.

2.3. Multi-wavelength pyrometry technique

The MW pyrometer used in this work is an FMPI SpectroPyrometer (FAR Associates, OH, USA). The FMPI can resolve temperature and spectral values for signal strength (equivalent to the emissivity under the assumption of target homogeneity) simultaneously from the measured target intensity and also provides a tolerance, an instantaneous measure of the accuracy of the reported temperature. Nominally, this device

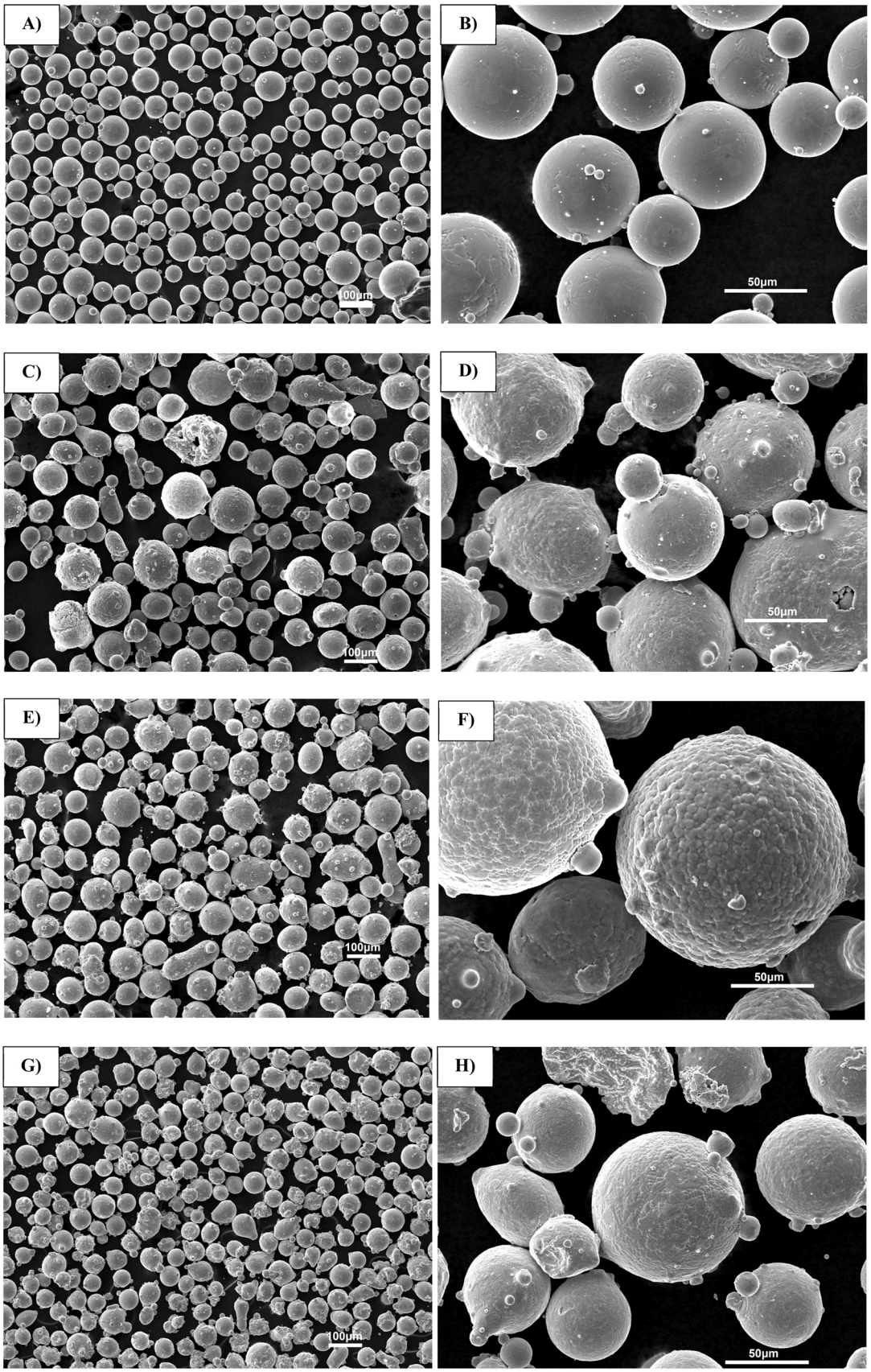

Fig. 1. Low (100X) and high (500X) magnification SEM images acquired for the stock powders: A) and B) for Ti6Al4V, C) and D) for TiAl, E) and F) for 316 L, and G) and H) for IN625.

Table 1
Particle size distribution of powder feedstocks.

Powder	PSD Range (μm)	d10 (μm)	d50 (μm)	d90 (μm)
Ti6Al4V	45-106	50	67	100
TiAl	45-150	51	79	128
316 L	45-106	55	74	104
IN625	45-106	47	70	106

Table 2
Chemical composition of powder feedstocks.

Material	Vendor	Chemical Composition (wt%)
Ti6Al4V	AP&C	Al 6.39, V 3.93, Fe 0.20, O 0.08, C 0.02, N 0.02, H 0.002, Y < 0.001, Other total < 0.20, Ti Bal
TiAl	Praxair	Al 34.5, C 0.005, Cr 2.5, Fe 0.03, H 0.002, N 0.01, Nb 4.8, O 0.1, Other total < 0.1, Ti Bal
316 L	Carpenter	C 0.021, S 0.005, Si 0.62, P 0.007, O 0.02, N 0.10, Ni 12.70, Mo 2.41, Mn 0.58, Cu 0.03, Cr 17.73, Fe Bal
IN625	Praxair	Al 0.06, B < 0.001, C 0.02, Co 0.10, Cr 21.38, Cu 0.02, Fe 4.0, Mn 0.03, Mo 9.09, N 0.009, Nb+Ta 3.72, O 0.0126, P 0.002, Se < 0.005, Si 0.06, Sn< 0.001, Ti 0.06, Ni Bal

operates by capturing the radiant flux or intensity of the target (small area or spot) in the 900–1700 nm spectrum. The lower 1080 nm limit for the spectrum of the FMPI is set by Planck's law for the lower process temperatures and the upper limit by the MW pyrometer's detector sensitivity. The raw spectral intensity data is captured by the device and then corrected by employing a radiometric calibration as detailed below. To obtain the intensity across the spectrum, the instrument uses a diffraction grating which separates and projects the intensity at each wavelength in the device's range onto an Indium-Gallium-Arsenide (InGaAs) linear photodetector array. Employing this array, the intensity values are simultaneously captured at distinct but closely spaced (1.56 nm) wavelengths. These hundreds of discrete wavelength/intensity pairs, with the optical path and detector radiometrically calibrated, are used to mathematically construct a multitude of virtual pyrometers. These virtual pyrometers and associated analyses can be used to determine temperature and emissive behavior across the spectrum of the detector even when the emissive behavior is non-gray [23,24,28,29]. Further, as detailed in works by Felice [23,30], the radiometric calibration is used to correct the intensity values which are subsequently used to compute a temperature matrix employing the ratio pyrometry form of Planck's distribution law (Eq. 1 below) for the multiple intensity-wavelength pairs collected:

$$T = \frac{C^{'}\left(\frac{1}{\lambda_2} - \frac{1}{\lambda_1}\right)}{\ln R - 5\ln(\lambda_2/\lambda_1)} \tag{1}$$

The temperature of the target is obtained by averaging and consensus of the values computed in the temperature matrix while the tolerance is calculated as the standard deviation of these values. During this process, checks for non-graybody behavior and corrections to the temperature matrix are performed [23]. Further details of this MW pyrometric technique are described in multiple works [22,25,30]. Once the target temperature is computed, the FMPI uses this consensus temperature to calculate spectral values of emissivity over the active spectrum using Planck's distribution law solved for emissivity (Eq. 2):

$$\varepsilon_{(\lambda)} = \frac{L\lambda^5\left[e^{hc/\lambda k_B T} - 1\right]}{2hc^2} \tag{2}$$

Then, along with the measurement of the temperature and its tolerance, the FMPI reports the signal strength at the default wavelength of 1500 nm. This wavelength is chosen by the manufacturer for reporting as it is centrally located within its measurement range and not affected by emission and absorption effects caused by water vapor in the region from 1347 to 1415 nm. Irrespective, the device stores all values of spectral signal strength in * .dat files for each observation made.

The radiometric calibration of the FMPI was performed against a NIST traceable conical IR-563 blackbody source (Infrared Systems Development Corporation, FL, USA). The procedure involved allowing the blackbody source to heat up and equilibrate at a specified temperature value at which the FMPI was calibrated. For the experiments reported in this work, the blackbody source temperature employed for calibration was 1000 °C. Except for IN625, the calibration of the FMPI prior to experiments was done by placing the blackbody source inside an argon (Ar) flooded glovebox enclosure (LC Technology Solutions, Inc., MA, USA) to maintain the environment to < 1.0 ppm O_2. For IN625, the calibration was done with the blackbody placed in ambient conditions. This different calibration resulted in peaks appearing in the spectral region from 1347–1415 nm for IN625, which correspond to the effect of water vapor in the ambient air, as previously described in [25]. The FMPI disregards this spectral region during the temperature calculation, but it is shown here (in the following IN625 results) to show the entire range of the measurements although this region should be ignored. Also, the calibration was performed including all the elements of the optical path, thus accounting for the slight loss in transmission of ~6% from the quartz glass. Metallization of the quartz viewport can be of concern for the calculation of temperature and propagate into the calculation of signal strength if it exhibits spectral selectivity. Nevertheless, calibration checks before and after experiments, visual inspection of the quartz windows, and the consistency of the measurements indicated that metallization was prevented in the setup used for experimentation [25].

As with any optical measurement thermometry technique, spatial averaging of intensity is performed over the target area with temperature measurements that are skewed towards areas of high intensity for targets that are not thermally homogenous, as recently shown [22]. In addition, in the normal operation of the MW pyrometer, temporal averaging is controlled by the dynamically adjusted exposure time. In our experience using the FMPI in PBF AM, typical exposure times are in the range of 0.012 seconds during preheating to 0.006 seconds during melting [22].

As described by Terrazas *et al.* [22] and based on the analysis by Ruffino [31], the signal strength measured by the FMPI is equivalent to the target (or material's) emissivity when the following two conditions are fulfilled: 1) physical phase, thermal, chemical and morphological uniformity of the 2.7 mm measured region, and 2) full accounting and calibration of the optical path without temporal variations arising from stray sources of absorption, reflection, or emission. Our prior works demonstrated that condition 2) is met for the experimental setup presented [22,25]; for example, Fernandez *et al.* demonstrated the unaltered calibration of the FMPI device before and after experimentation and showed the negligible effect (of the reflective environment on the measurements made during melting of pure copper [25] through calculation of a maximum reflective ratio contribution of 0.125%. Nonetheless, regarding condition 1), during some of the process stages of the PBF-EB process, the traveling electron beam heat source results in the development of non-isothermal conditions of the target as the measurement region undergoes non-uniform heating profiles and phase transitions as depicted in the schematic in Fig. 2. This non-uniform heating can also result in rapid changes in surface morphology impacting the target's emissivity as the surface transitions from solid powder to liquid (for example a turbulent liquid with rapidly changing surface morphology), and back to a solidified surface. The conditions during the melt scanning step (Fig. 2 B)) necessarily lead to the coexistence of multiple phases (powder, liquid, solid) and/or thermal gradients which can cause bias in the temperature values calculated as influenced by the brighter region, depicted as A2 or liquid in Fig. 2 B), whereas the signal strength or emissivity is biased by the lower intensity of A1 and A3. That is, Ruffino demonstrates that the technique measures the peak temperature of the region, while emissivity might be unresolved given the various sources of intensity coexisting in a target. Thus, during non-isothermal conditions experienced within the target, the

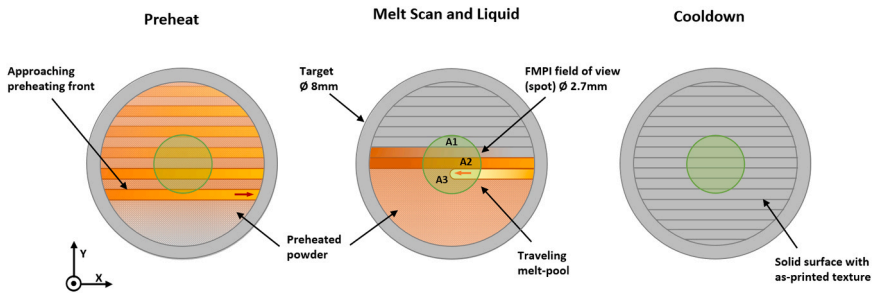

Fig. 2. Schematic showing the thermal conditions experienced during A) preheating, B) melt scan B), and C) solidification/cooldown process stages, to indicate the variability in the target, particularly as shown in B) where the coexistence of multiple physical phases (powder, liquid, solid) causes bias in the temperature calculation towards the region including the melt-pool (A2).

signal strength might not accurately represent the emissivity of the target. Nevertheless, during process stages that are not very thermally transient (such as cooldown), the signal strength calculation can be considered as the emissivity of the target. While not resolved during highly transient process phases, the tolerance calculated for each temperature can also estimate the confidence of the signal strength/-emissivity values computed.

2.4. FMPI exposure time limits

The methodology employed systematic changes to the exposure time limits (maximum and minimum) for the FMPI pyrometer to measure the detailed thermal emissive behavior at the various process stages; these exposure time limits were set directly in the configuration file used by the device. To be clear, the exposure time is simply the amount of time required for the detector of the FMPI to receive sufficient radiation to make a measurement (determined by an internal algorithm); all wavelengths of the radiation are sampled at the same time. The procedure of specifying exposure times in the configuration file allowed for data acquisition during transients that would otherwise not be captured due to the required time of the FMPI algorithm used to determine a new exposure time and then collect data at that time. Table 4 provides a listing of the exposure time limits (in sec) and the PBF-EB melt scanning parameters employed for the data reported in the results. These changes enabled acquisition of measurements in the very transient regions of the melt scan and liquid phases for the four alloys studied. This contrasts with the automatic exposure time adjustments made by the MW pyrometer in its standard operation. As described in [23–25], during standard use, the algorithm employed by the FMPI pyrometer adjusts the exposure time values (within the limits of 4 μs to 8 seconds) based on the brightness or intensity of the target being measured to ensure an adequate signal-to-noise ratio and to avoid saturation of the detector. For traditional manufacturing processes, targets observed are not as thermally transient as occurs during PBF, and thus, very high-speed acquisition was not a design consideration in the auto-exposure algorithm. The transient nature of processing in PBF causes intensity changes that might be too fast to capture; hence limiting the exposure time values provided faster reaction times for the MW pyrometer to capture data in regions of interest.

2.5. Electron beam powder bed fusion

The use of the PBF-EB as a platform for experimentation provided a pristine environment that would allow the experiment to isolate the thermal emissive behavior from other process effects, hence providing unique insights into the fundamental emissive behavior of materials during processing. In PBF-EB, the powder bed preheating causing weak sintering of powder particles, the larger melt-pool size (measured at ~900 μm or larger versus the nominally ~450 μm) caused by scaling down of the scan velocity and power delivered, and the controlled vacuum conditions, provide for a more stable process that is not occluded by the plasma plume, process ejecta, and the chamber gas and other constituents that are prevalent in PBF-LB.

PBF-EB processing was conducted in two Arcam PBF-EB systems (GE Additive, Sweden): S12 and A2X models. Ti6Al4V was processed in the S12 and the other three materials in the A2X. The specifics of these systems have been detailed elsewhere [32–35]. For the experiments performed here, Fig. 3 A) and B) show the MW pyrometer attached to the chambers of both the S12 and A2X PBF-EB systems. The FMPI unit (described in Sections 2.3 and 2.4), coupling fiber and optic, and the vacuum extension rated tube (described in Section 2.2) are visible in the photographs. In brief, the PBF-EB process employs a thermionically emitted electron beam operating at a voltage potential of 60 kV with a maximum output of 3 kW. Magnetic coils steer and focus the beam achieving a beam diameter that can dynamically vary from 200–1000 μm but that is nominally focused at ~250 μm. The process is performed at elevated temperatures through an initial preheat of the deposition substrate, and by preheating each spread powder layer using a defocused beam prior to the selective melt scanning step. Preheating is possible by the fast actuation of the magnetic coils. A heat shield enclosure made of brushed stainless-steel walls helps to maintain the elevated temperature through heat radiation and reflection into the powder bed. For these systems, turbo molecular pumps and a constant helium bleed are used to maintain controlled vacuum conditions (2.0×10^{-3} mbar) throughout processing.

2.5.1. Measured target

The monitored spot of the FMPI is ~2.7 mm in diameter, indicated schematically as the green dot in Fig. 3 C). For the experiments reported here, the FMPI measuring spot was centered on the location within the powder bed onto which a single cylinder, the target geometry, measuring 8 mm in diameter was deposited. The height of the cylinder was set at 1.5 mm to enable capturing data for at least ten layers given the layer thickness (50 μm for all materials, except 70 μm for Ti6Al4V). Other rectangular parts were also built alongside the target cylinder, to maintain the elevated temperature during processing, as is commonly necessary in PBF-EB processing. For all experiments, the target geometry was melt scanned first in a single hatch then followed by a second hatch over the rest of the rectangular parts. In addition to the experimental setup photographs, Fig. 3 C) also shows a schematic representation of the general build layout. In the configuration shown, the cylinder was offset from the center of the build substrate by 44 mm to the right, and 6.5 mm down (coincident with the location of the green dot).

2.6. Melting strategy and volume energy delivery

During melting, the Arcam PBF-EB process employs the dimensionless parameter called speed function to maintain a constant energy delivery by the electron beam. The exact form of the speed function parameter has not been disclosed in literature, but in general, it relates

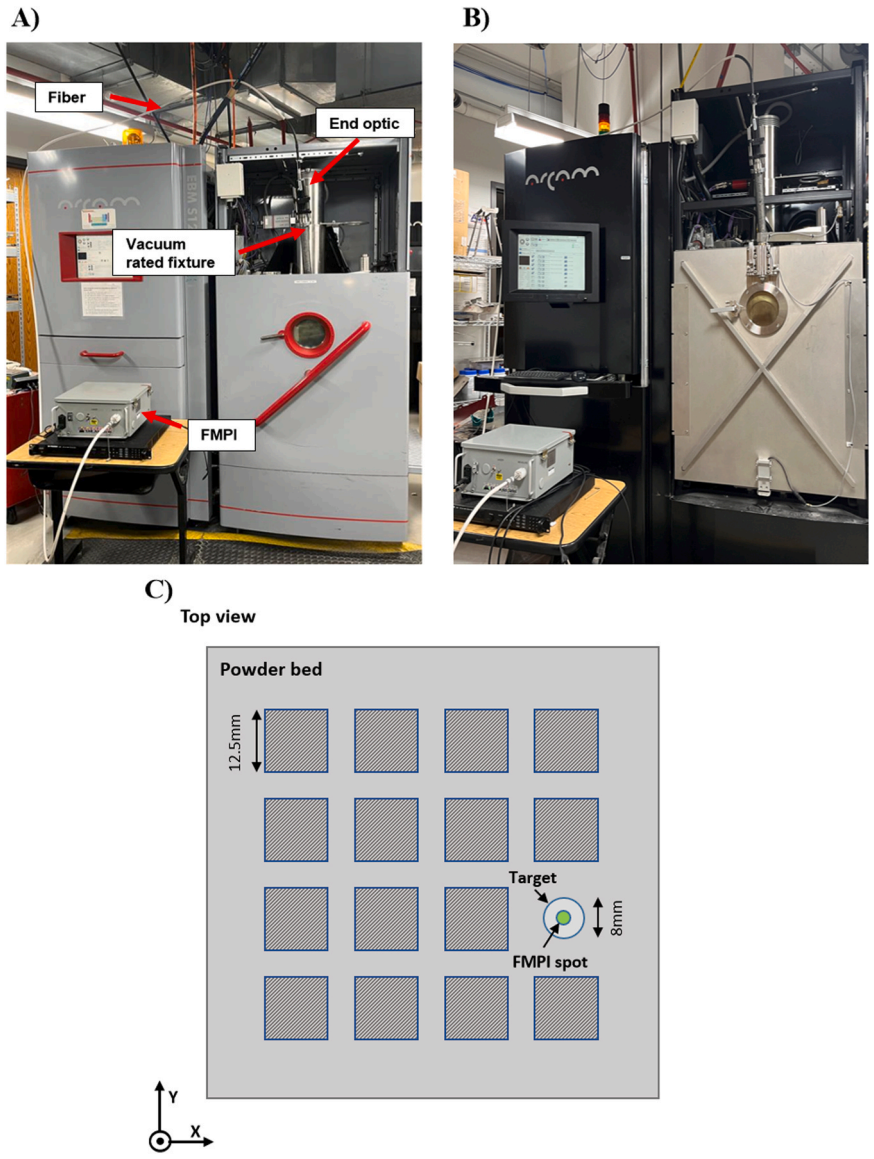

Fig. 3. A) and B) show the Arcam S12 and A2X PBF-EB systems, respectively. C) Schematic showing the general layout employed during experiments (shown to scale). Green dot represents the ~2.7 mm diameter spot on which the FMPI was aligned concentric to the deposited 8 mm diameter cylinder, relative to the center of the substrate.

values of beam current and speed. For our work, to successfully measure emission during melt scanning and at the liquid (molten) state, the speed function parameter was modified from the nominal values (Table 3), to slow down the melt scanning of the electron beam, while maintaining a near constant energy delivery. Modification of the speed function parameter influenced the beam scanning speed and current as described elsewhere [36,37]. In summary, this change to the speed function had the effect of also scaling down the beam speed (mm/s) and beam current (mA) parameters. In our work, the model presented by Scharowsky *et. al.* [38] was used to compute the volume energy (E_v) at the maximum operating current and nominal values of beam speed (v) and speed function parameter following Eq. 3 below. Then, holding the value of E_v constant, all other parameters were scaled down based on the percent change of speed function, to compute the approximate value of beam speed and current (average and max) values. In Eq. 3, P (watts) was calculated by multiplying beam current values (mA) times the accelerating voltage that is fixed at 60 kV. The hatch spacing h_s (or line offset parameter for Arcam), and layer thickness l_z parameters were also fixed for each material. In general, this strategy resulted in the formation of a larger melt-pool that existed temporally for longer at near isothermal

Table 3
Nominal PBF-EB process parameters for each material.

Material	Preheat Temp (°C)	h_s (mm)	l_z (mm)	Speed Function	Beam speed (mm/s)	Beam current (mA)		Volume Energy (J/mm3)
						Max	Avg	
Ti6Al4V	760	0.1	0.05	98	4530	21	15	55.6
TiAl	1100	0.2	0.07	10	1600	21	12	56.3
316 L	1000	0.1	0.05	50	4530	20	15	53.0
IN625	950	0.2	0.05	40	1205	15	14	74.8

conditions in the melt scanning and liquid process stages, thus allowing increased data acquisition during these highly transient processing phases. The list of nominal process parameters per material is listed in Table 3 whereas Table 4 shows the speed function values employed to slow down the beam, with approximated speed and current values.

$$E_v = \frac{P}{v \bullet \quad h_s \quad \bullet l_z} \tag{3}$$

As detailed in prior works [22,25], the use of nominal parameters for melt scanning in PBF-EB, coupled with the self-adjusting, target intensity-based algorithm of the FMPI, resulted in challenging conditions for capturing sufficient data in the highly transient process stages (melt scanning and liquid). Nevertheless, the unique experimental approach employed, consisting of the combination of reduced beam scanning speed of the PBF-EB systems and changes to the exposure times of the FMPI, overcame this challenge enabling near continuous measurements to be made without loss of calibration. The results presented in the following highlight the differences in processing required for each material but also the effectiveness of the technique to capture data in all process stages of interest.

3. Results and discussion

For the discussion that follows, it is instructive to recall that when the two conditions as mentioned in Section 2.3 are met (i.e., uniform phase, temperature, chemistry and morphology in the measurement region and calibrated instrument and optical path without temporal changing calibration), the signal strength measured by the FMPI is equivalent to the emissivity of the target or the material under study. In this section, all results will be reported as signal strength / emissivity, and the associated discussion will indicate when the measurements can most reliably be considered the emissivity of the material under study.

3.1. Temperature measurements

Figs. 4 through 7 parts A) show plots for the temperature (black plot with black empty markers) and signal strength / emissivity at 1500 nm (gray plot with gray empty markers) measured by the FMPI for ten layers of fabrication using Ti6Al4V, TiAl, 316 L, and IN625, respectively. In these plots, each peak represents the deposition of a single layer transitioning through the preheating, melt scanning, liquid, and solidification/cooldown process stages. Horizontal red lines with temperature labels were added in these plots to indicate the reported melting range (T_{Low} for the lower limit of the melting range, and T_{High} for the higher limit of the melting range) for each alloy [39–41]. The FMPI resolves the temperature and signal strength of the target using the previously described approach as long as the optical path remains unchanged. The zoomed views in Figs. 4 through 7 parts B) show the profile of a single melt event (peak) showing that the MW pyrometry technique used is capable of resolving temperature values in distinctive process stages that include the preheating, melt scanning, liquid, and solidification/cooldown (hereafter referred to as cooldown).

It should be noted that the accuracy of the MW pyrometry technique has been shown in previous works against contact sensors including immersion thermocouple measurements during investment casting of nickel-based alloys [26] showing average deviations of ~3 °C over days of operation, and in our prior work using sheathed thermocouples embedded in a heated powder bed of pure copper [25], showing comparable measurements by both the FMPI and thermocouples, deviating by only ~2 °C. The accuracy of the FMP2, which relies on the same MW pyrometry technique, versus standard tungsten lamps, to within a few degrees Celsius, was also shown in [27] in spite of spectral variations in the measured emissivity due to aging of the lamps.

The plots for Ti6Al4V in Fig. 4 show that while data are captured during the preheat step, the acquisition of data is reduced during melt scanning, only capturing information at elevated temperatures approaching the melting point. Similarly, the data is sparse during the high transient solidification stage but then increases again upon the final onset of cooldown. The expanded view for the temperature plot for Ti6Al4V (Fig. 4 B)) shows a characteristic double peak feature which can be attributed to the initial melt scan of the contour for the target part followed by the increase in temperature as the beam scanned through the hatch area of the target geometry. The oscillations exhibited from t~4324 seconds capture the back-and-forth travel of the electron beam during scanning of the target area.

The temperature and signal strength / emissivity plots for TiAl, in Fig. 5 A) shows the progression for ten layers or melt cycles and part B) shows the data for a single melt event. Similar to previous observations, abundant data is captured in the preheat and cooldown stages, but it is sparse during the transient melt scanning and liquid process stages.

The plots for 316 L (Fig. 6 B)) and IN625 (Fig. 7 B)) show that there are two distinctive preheating phases prior to the melt scanning where signal strength / emissivity changes are also evident. Also, the plots for TiAl and IN625 show that following the melting event (liquid phase), the frequency of measurements during cooldown is high, which can also be attributed to the post heating used for these materials to keep the temperature high prior to spreading of a new layer of material. Furthermore, the plot for 316 L (Fig. 6 B)) shows that the melt scanning settings used for this material allowed increased frequency for capturing the temperature ramp up during this process stage.

3.2. Signal strength / emissivity measurements

The signal strength / emissivity values reported by the FMPI at the wavelength of 1500 nm are shown in the scatter plots (Fig. 8) as a function of time in the four process stages color-coded (preheating = yellow, melt scanning = red, liquid = green, and cooldown = blue) for A) Ti6Al4V, B) TiAl C) 316 L, and D) IN625. An alpha or transparency value of 0.75 was used for all markers to improve the visibility of overlapping data.

The plots show the aggregated data for ten layers using a time zero datum selected by defining the start of the preheating sequence for each layer as t = 0 seconds. By superimposing the data for ten layers, the data provides remarkable insight into the overall thermal radiative-emissive behavior with discernable and similar patterns for the signal strength / emissivity in each of the four processing stages. Although when overlayed the general patterns appear similar, there are differences between them, denoted by temporal variations in gray and non-gray behavior of the emitting material, as will be discussed in the results and discussions that follow. It should also be noted that slight variations in the duration of the preheating for each layer, due to a temperature-control preheating algorithm used in the Arcam PBF-EB process, caused some shifting or

Table 4
Parameters employed in PBF-EB and MW pyrometer.

Material	Speed Function	Beam speed (mm/s)		Beam current (mA)		Volume Energy (J/mm3)	FMPI exposure time (sec)	
		Max	Avg	Max	Avg		Max	Min
Ti6Al4V	12.25	566	404	2.6	1.9	55.6	0.010	0.003
TiAl	1.25	560	320	2.6	1.5	56.3	0.010	0.003
316 L	20	1903	680	20	15	53.0	0.012	0.012
IN625	5	421	301	2.6	1.9	74.8	8.000	4e-6

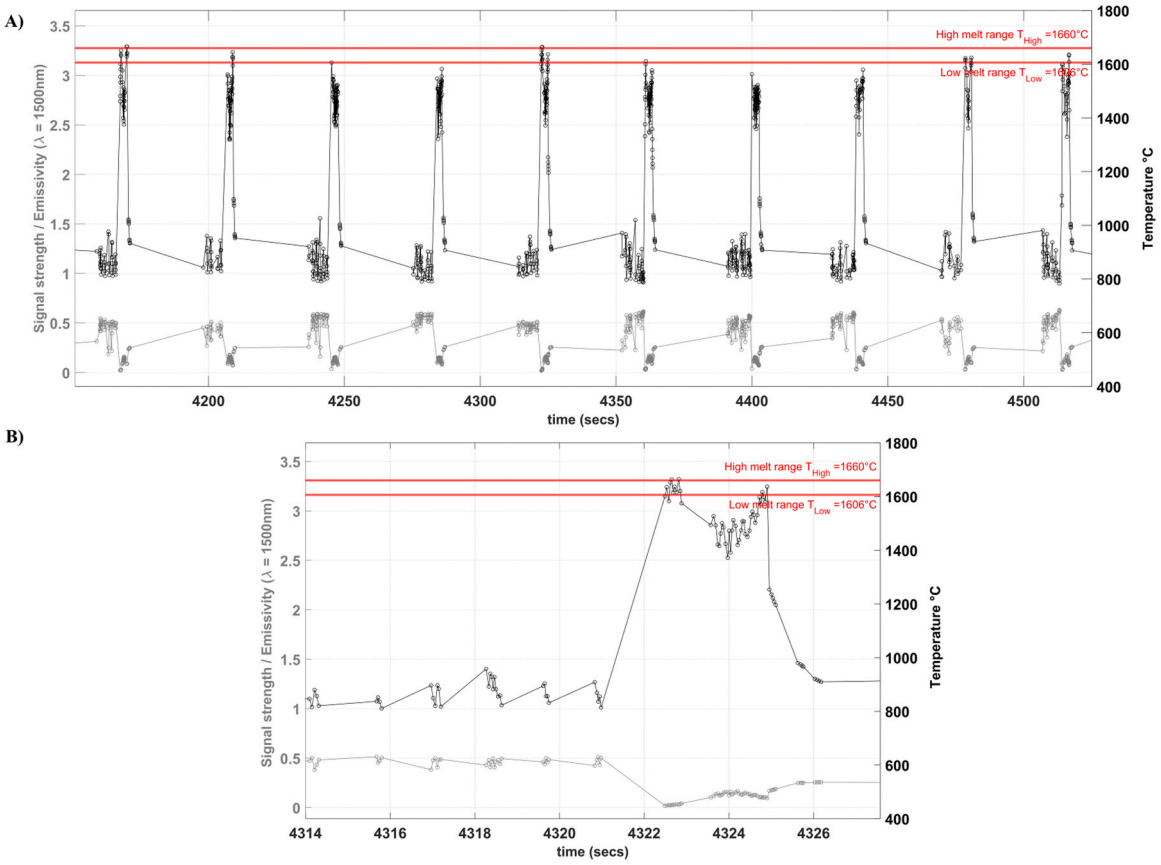

Fig. 4. Temperature and signal strength / emissivity plots for Ti6Al4V; A) full progression of ten (10) layers or melt events. B) plot for single melt event.

offsetting of the data captured during melt scanning, liquid, and cooldown. This offset is evident in the plots for Ti6Al4V and IN625 and indicated by black arrows. Also noteworthy is the extended regions for the cooldown for TiAl and IN625 (Fig. 8 B) and D)), which develop from a post-heating sequence applied throughout the powder bed after selective melting. Finally, the signal strength / emissivity dependence on temperature is seen for all materials during the preheating process stage (yellow markers in Fig. 8) with values that oscillate (increase and decrease) as preheating fronts cross the target due to the raster scan pattern of the electron beam.

For Ti6Al4V, the plot in Fig. 8 A) shows that signal strength / emissivity values cluster in a region spanning from approximately 0.20 to 0.60 during the preheating stage. At least four specific subregions can be denoted with spacings that correlate with the scanning of the electron beam. The two preheating phases (normally applied during PBF-EB processing) are seen from t ~0–4.5 seconds (first preheat) and from t ~4.5–7.5 seconds (second preheat). The temperature dependence is observed as signal strength / emissivity generally increases from ~0.25 to ~0.60 as temperature increases during pre-heating. During melt scanning, the signal strength / emissivity measured drops to ~0.13 whereas during the liquid stage it reaches its minimum at ~0.03. Then, upon cooldown, the signal strength / emissivity increases into a stable region at ~0.25.

The signal strength / emissivity behavior for TiAl is shown in the plot in Fig. 8 B). The preheat phase lasts about 8 seconds, during which time signal strength / emissivity ranges from ~0.46 to ~0.67 following the increasing trend as temperature increases. Then the melt scanning stage starts with the signal strength / emissivity making an excursion from ~0.53 until reaching the minimum at the liquid stage of ~0.15 and then stabilizing at ~0.20. During the cooldown stage, the signal strength / emissivity climbs back and remains stable at ~0.35. This cooldown stage extends for about 11 seconds.

Next, the signal strength / emissivity for 316 L is shown in Fig. 8 C). This scatter plot shows pockets of data during the preheating stage that are due to the combination of the electron beam scanning and FMPI settings employed. Two distinctive regions of preheating are observed, with the first lasting until about 12 seconds, immediately followed by the second one that ends at about 22 seconds. The first preheating stage denotes eight consecutive signal strength / emissivity data clusters that span from ~0.41 to ~0.59, while the secondary preheat phase is characterized by a range of signal strength / emissivity values from ~0.33 to ~0.57. The material displays a similar increasing trend for the signal strength or emissivity, with values that rise as temperature increases locally during the preheat. Following the preheating sequences, the melt scan stage spans a region in which measured signal strength / emissivity drops from ~0.46 to a minimum of ~0.14 upon reaching the liquid state. Then the signal strength / emissivity values during cooldown move from ~0.20 to a stable ~0.25.

For IN625, the signal strength / emissivity behavior is shown in Fig. 8 D). The plot shows a preheating stage that lasts ~13 seconds and ranges in signal strength / emissivity from ~0.46 to ~0.60 but aggregates more strongly at ~0.55. In the preheating step, the signal strength / emissivity values observe a dependence on temperature as stated previously for the rest of the materials. Then during melt scanning the signal strength / emissivity makes an excursion to values ~0.25, reaching a minimum during the liquid stage of ~0.17. Finally, during the cooldown stage, the signal strength / emissivity climbs to values just above ~0.30 and stays relatively constant through the duration of this stage lasting approximately 20 seconds.

The set of plots shown in Fig. 8 demonstrate that, for the four materials presented, the signal strength / emissivity exhibits a highly dynamic behavior while transitioning through different process stages. These changes in signal strength / emissivity are also highlighted in Table 5, represented as percent changes of average values of signal

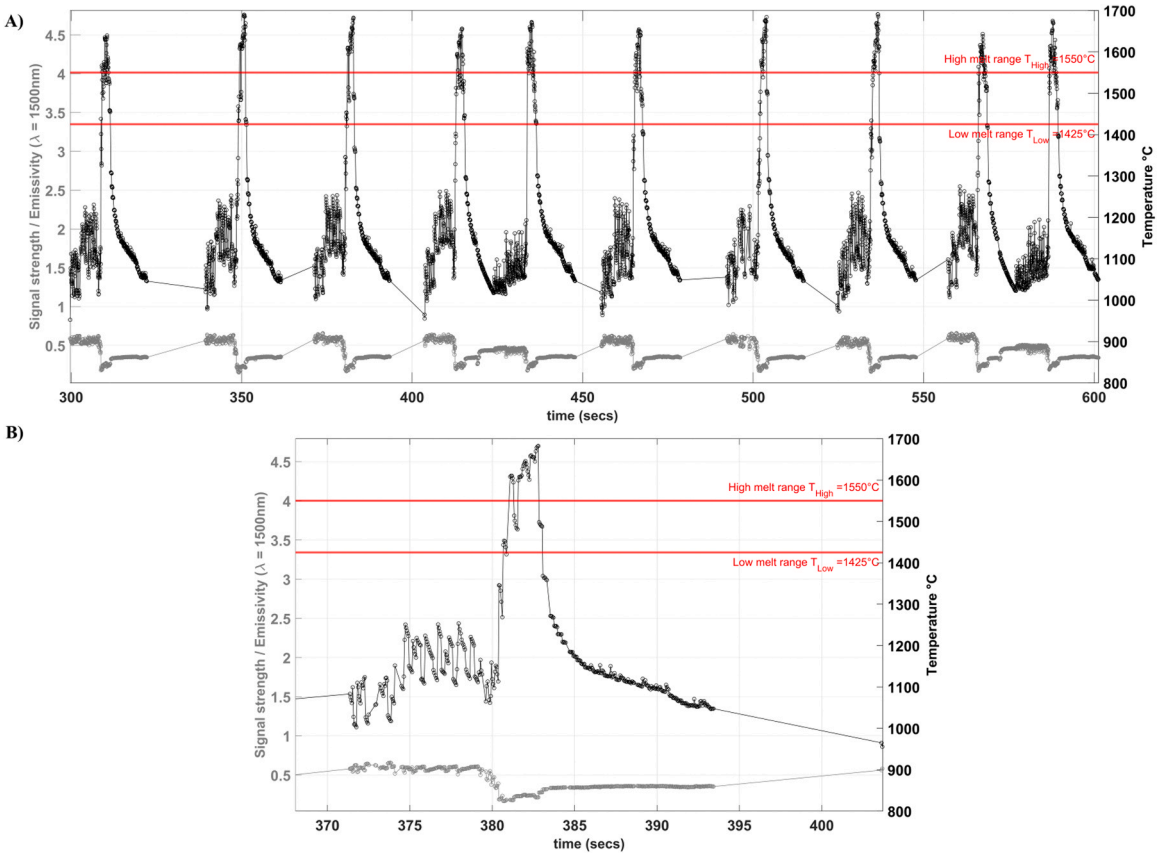

Fig. 5. Temperature and signal strength / emissivity plots for TiAl; A) full progression of ten (10) layers or melt events. B) plot for single melt event.

strength / emissivity between stages. It is noteworthy to highlight the drastic variations for the signal strength / emissivity during processing as depicted in Fig. 8, which the authors hope benefits the overall additive manufacturing community in understanding the physical behavior of emissivity of metallic materials during processing. For example, as shown in Table 5 for Ti6Al4V, over a 300% change in signal strength / emissivity is experienced when transitioning from liquid to cooldown (after solidification). These drastic changes in emissive behavior highlight the potential limitations of most approaches for radiation thermometry described in literature, where the emissivity of the observed target is incorrectly considered invariant.

Further, the data presented in Fig. 8 shows with remarkable detail the dependence of each material's thermal emissive behavior on its processing conditions with notable and distinct variations resulting from changes in phase and morphology (from solid powder to liquid to structured solid). For all materials, the data measured during the preheating stage shows the signal strength / emissivity dependence on temperature shown as values that oscillate locally, increasing as a preheating front approaches, and then decreasing as the front moves away. By contrast, results provided in literature, including comprehensive compendiums such as the Thermophysical Properties of Matter (TPRC) [20], indeed provide details of the emissive behavior for various materials, but this is usually done for carefully and extensively prepared solid samples with surface roughness modifications and thermal treatments and that remain unaltered in shape for the most part. This is also the case for results presented in the wider field of thermometry; for example, data for a variety of prepared samples for various materials are presented in [42–45]. The data from these sources are not obtained from in situ conditions experienced by a material during processing, whether by PBF or some other processing method in which the material changes phase and form. The approach presented here captures the dynamic emissive behavior in situ and without the need for extensive preparation of the samples. This clearly differentiates the results in literature from those reported here.

While improvements to the MW pyrometry technique are still necessary to capture the transitions in the emissive behavior in greater detail, the current results in Fig. 8 show the overall trends clearly. The data highlights the highly dynamic transitions that occur with materials during PBF processing that contrast with the traditional assumption of invariance. As discussed in Section 2.3, it is instructive to recall the two conditions that impose a limitation on the certainty to which the values presented in Fig. 8 can be considered the emissivity of the target; while the results are dependent on the material, in general the signal strength can be considered equivalent to the emissivity of the target for measurements that were taken of a uniform temperature target (i.e., that would occur, for example, with the electron beam turned off).

3.3. *Spectrally variable emissive behavior*

Although perhaps not widely known by the AM community, it is well established that emissivity has a spectral nature for metals which in general monotonically decreases as the wavelength increases [6,20]. Our work shows this spectral nature in the active range of the FMPI (1080–1637 nm) for selected data points for each material in the four process stages, preheating (yellow), melt scan (red), liquid (green) and cooldown (blue), employing the color-coded plots in Figs. 9 through 12. The selected data points correspond to the median value out of all the observations made for each process stage (i.e., from the aggregated data for ten layers). For these plots, the central line shows the spectral data while the light region shows the uncertainty upper and lower bounds (i.e., uncertainty added and subtracted from the values in the central line; details of the uncertainty calculation are presented in Appendix A.). Also, default y-axis limits have been selected to enhance visibility of the spectral change of signal strength / emissivity for each plot(i.e. y-axis

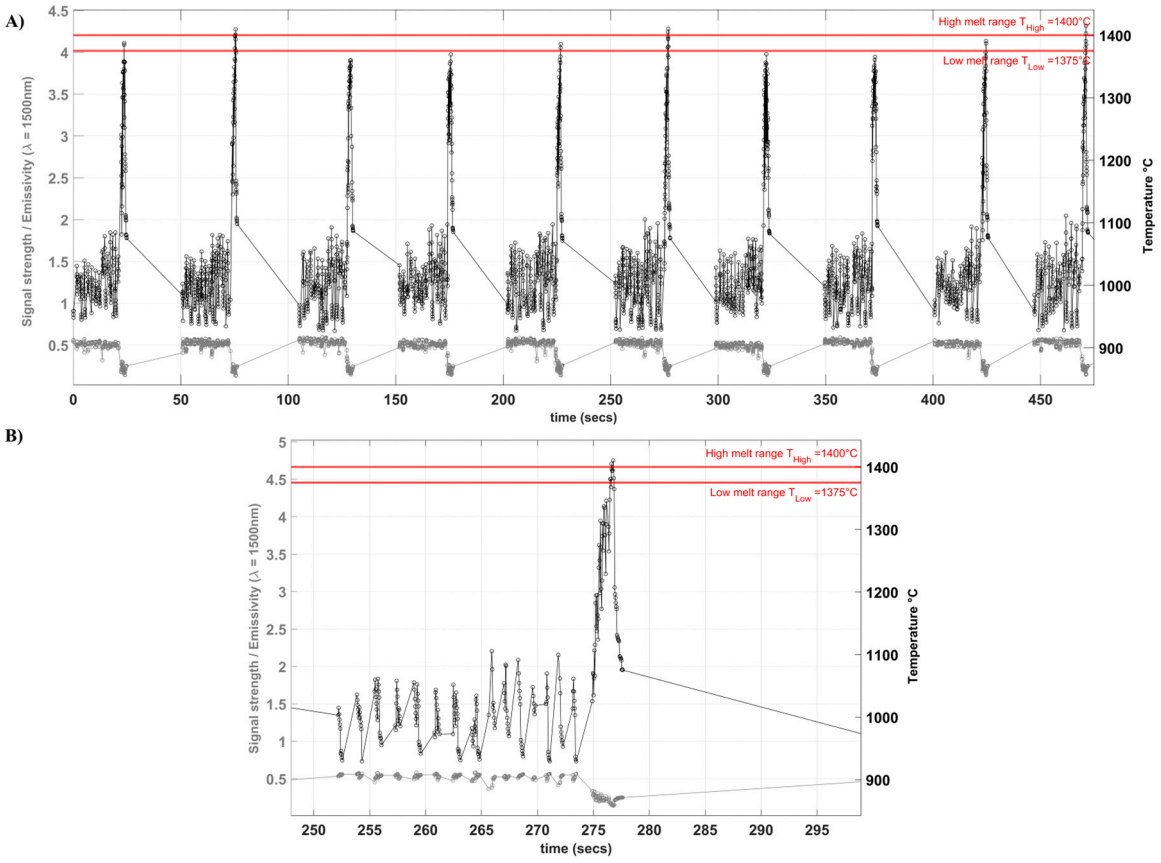

Fig. 6. Temperature and signal strength / emissivity plots for 316 L; A) full progression of ten (10) layers or melt events. B) plot for single melt event.

limits vary from plot to plot).

In general, the spectral distribution plots exhibit monotonically decreasing trends as the wavelength increases, consistent with the behavior that has been described for various metallic materials under different processing conditions [6,20,46]. Specifically for each material, the plots show that for Ti6Al4V, the greater variability in measurements (i.e. larger error bounds) occurs for the preheating and melt scanning stages, with otherwise small error bounds for liquid and cooldown (Fig. 9). Similarly, for TiAl (Fig. 12), the largest variability is seen for the melt scanning and preheat stages, with small error bands for liquid and cooldown phases. In Fig. 11, the largest error bounds are shown in the melt scanning phase for 316 L stainless steel, with small error bounds for the rest of the process stages. Finally, Fig. 12 for IN625 indicates that the largest variability occurs for the melt scanning followed by the liquid; for this material, the error bounds for the preheat and cooldown are relatively small compared to the rest of the spectral plots. Also, for IN625, the peaks that appear in the spectral plots in the region from 1347–1415 nm develop since the calibration of the FMPI was not performed in an inert environment as was done for the experiments with the rest of the materials. These peaks, which develop due to water absorption in that range, are effectively discarded by the FMPI during the calculation for temperature and hence have no effect on the spectral signal strength / emissivity values outside this spectral region.

The results obtained indicate that, irrespective of the material, the highest variability generally occur within the preheating and melt scan process stages where the thermal conditions of the target are the most non-isothermal and transient. Given the non-equilibrium conditions occurring during melting, the non-homogeneous nature of the target causes more variability (and therefore uncertainty) to develop during the melt scanning stage. As detailed in our prior works [22,25] and expanded here, the non-isothermal conditions of the target arise from the interaction of the traveling heat source (electron beam) causing the coexistence of multiple physical phases (powder, liquid and solid) during the melt scanning that can bias the temperature calculation towards areas of high intensity, as depicted in the schematic in Fig. 3 B). This non-uniformity of the target during highly transient phases (melt scanning and liquid) leads to higher tolerance (standard deviation of temperatures measured by the FMPI) values which drive both uncertainties in temperature and emissivity as calculated in Appendix A and listed in Table 6. By contrast, the variability calculated during the cooldown stage is the smallest for all materials, consistent with the observation that during this stage the target is a more uniform and stable solidified surface.

The large variation in the magnitude and spectral behavior of the signal strength / emissivity plotted in Figs. 9 through 12 is anticipated given the drastic changes in temperature, morphology (i.e., from grainy powder to reflective liquid), phase (i.e., solid powder, to liquid, to solid), and chemistry. Although chemistry was not a controlled variable in this work, chemistry variations indeed arise from compositional differences, and/or solute partitioning during the fast transient melting and solidification occurring in PBF AM, as detailed in various works [47–49]. Changes in chemistry due to evaporation of light alloying elements have also been documented for PBF AM processes [50,51]. The spectral plots in Figs. 9–12 indicate the high variability (non-grayness) in emissive behavior for each of the alloys; for example, observation of the emissive behaviors show that the preheat stage demonstrates the most gray behavior, while the cooldown stage is clearly spectrally varying for all materials. Overall, these figures demonstrate the difficulty with generalizing the emissive behavior for materials used in PBF as this behavior is highly dependent on temperature, phase, morphology, and chemistry.

3.4. Time variable emissive behavior

From further analysis of the data presented in Figs. 9 through 12, a

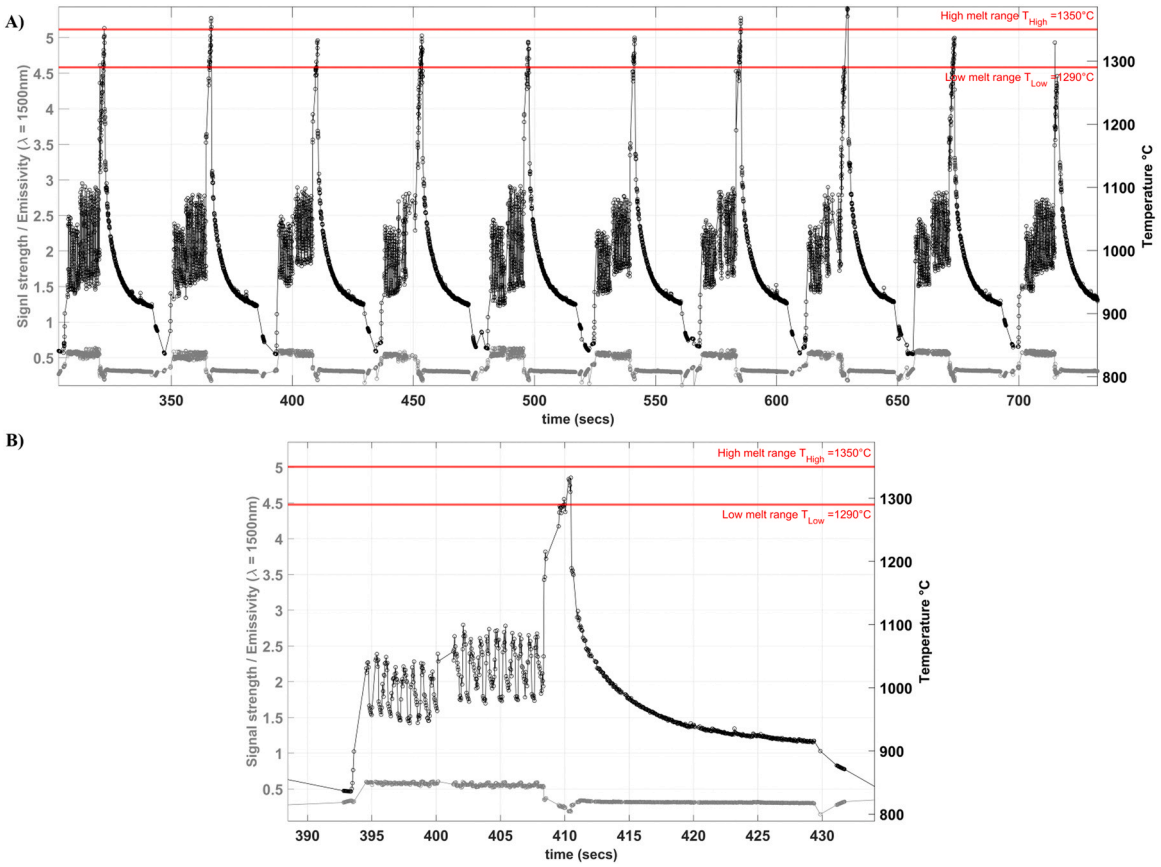

Fig. 7. Temperature and signal strength / emissivity plots for Inconel 625; A) full progression of ten (10) layers or melt events. B) plot for single melt event.

profound realization was also concluded that different emissive behaviors also occur at similar points in a material's evolution during processing. Using the values of signal strength / emissivity (i.e. spectral behavior) as a guide, specific observations were selected from the data to generate spectral signal strength / emissivity plots revealing the changing behavior of this parameter for similar temperatures occurring in each of the process stages of interest for each material. Figs. 13 through 16 show plots of spectral signal strength / emissivity detailing the occurrence of nearly gray and non-gray behavior for similar temperatures occurring across separate melt scans or layers, for each material. Temperatures selected for this analysis had a $\pm$ 5 °C range and corresponded to those measured in the four process stages as indicated for each material in the caption of the figures.

The plots in Figs. 13 through 16 detail the spectral behavior which can transition between gray and non-gray even when data points are measured at similar temperatures and in the same process stage (preheat, melt scan, liquid, or cooldown) but during different scans. This corresponds to making the same measurement but during different layers of a build, which considerably further complicates generalizing the emissive behavior of the materials during processing. This occurrence is more pronounced, for example for the preheat stage for TiAl (Fig. 14 A)) and for the cooldown stage in 316 L (Fig. 15 D)).

3.5. Implications for the practice of IR thermography

Considering the foregoing discussion and results presented, the authors intend these data to serve the AM community in two primary ways. First, these data should benefit fundamental understanding of the variation of emissivity during processing to both inform the fundamental physics of emissive behavior during the process as well as inform users of specific limitations of application of IR (single color), two-color, and other radiation thermometry methods in metallic PBF processing. As was shown throughout, emissivity is time and spectrally variable, and may oscillate between gray and non-gray from scan to scan. This presents an almost insurmountable hurdle when applying radiation thermometry methods that rely on a priori knowledge of emissivity or emissive behavior (i.e., single, or two-color methods) if accurate temperature measurements are desired. Second, the datasets are available upon request with the intent of benefiting the numerical modeling community in developing more accurate simulations of the PBF process.

A survey of the current literature on numerical modeling in PBF indicates the prevailing *status quo* in the community where arguably little consideration is given to the variations in the emissive behavior for materials in either modeling or experimental works – most probably due to a gap of fundamental emissive behavior information for PBF materials that the current work is intended to fill. While works such as that presented by Khairallah *et. al.* considered a variable emissivity for 316 L ($\varepsilon = 0.40$ for powder and $\varepsilon = 0.10$ for liquid) in the definition of a model to simulate the various physical effects occurring during melting in PBF-LB [52], various efforts such as those presented in [53] and [54] showed the use of a constant value of emissivity ($\varepsilon = 0.4$) for simulations of PBF-LB processing of IN625, not accounting for variations experienced due to phase changes. The work in [53] considered constant emissivity for a model of the combined radiation and convection boundary condition to simulate the melt pool development, and [54] employed the same assumption in the definition of the radiation heat loss term for a multi-mesh finite volume method. Similarly, [55] showed the use of a constant $\varepsilon = 0.04$ for a surrogate model of the laser melting process while the thermal behavior for 316 L was simulated also employing an $\varepsilon = 0.35$ in [56].

In addition to the use of constant values of emissivity in modeling, most works describing experimental techniques for monitoring in PBF AM have also resorted to the constant emissivity assumption, as referenced before [7–19]. Specifically, Boone *et. al.* presented an emissivity

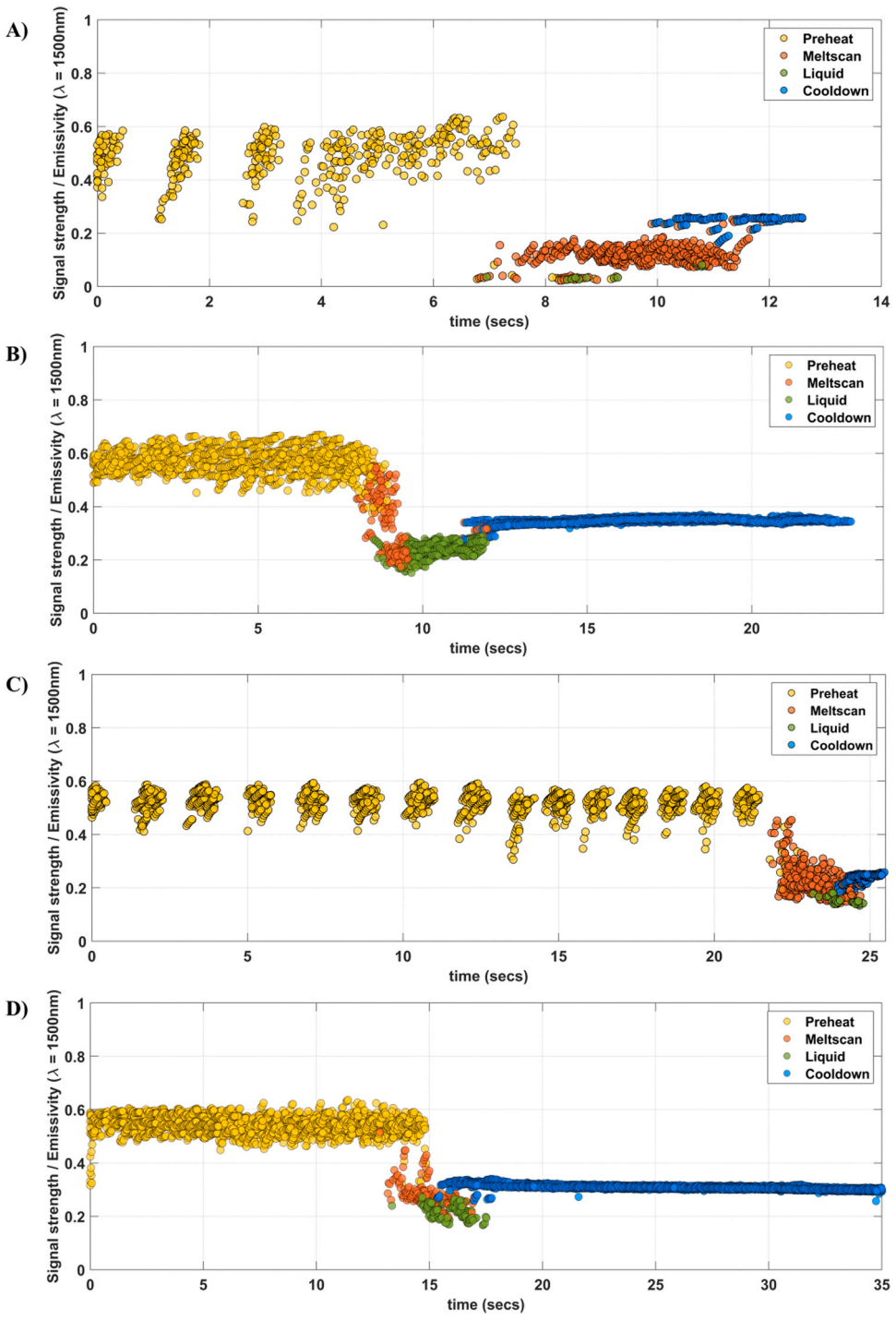

Fig. 8. Scatter plots for signal strength / emissivity (λ = 1500 nm) versus time for the four alloys studied. Color coding is used to indicate the processing phase for A) Ti6Al4V, B) TiAl, C) 316 L, and D) IN625. Plots show the superimposed, time-offset data for 10 layers.

Table 5
Percent change for signal strength / emissivity as material transitions in between process stages.

	Preheat to Melt scan			Melt Scan to Liquid			Liquid to Cooldown		
	Avg_{PHT}	Avg_{MLT}	% Δ	Avg_{MLT}	Avg_{LIQ}	% Δ	Avg_{LIQ}	Avg_{COO}	% Δ
Ti6Al4V	0.48	0.12	75%	0.12	0.06	50%	0.06	0.26	329%
TiAl	0.57	0.35	38%	0.35	0.24	33%	0.24	0.35	46%
316 L	0.52	0.22	57%	0.22	0.16	30%	0.16	0.25	61%
IN625	0.55	0.29	47%	0.29	0.22	24%	0.22	0.31	40%

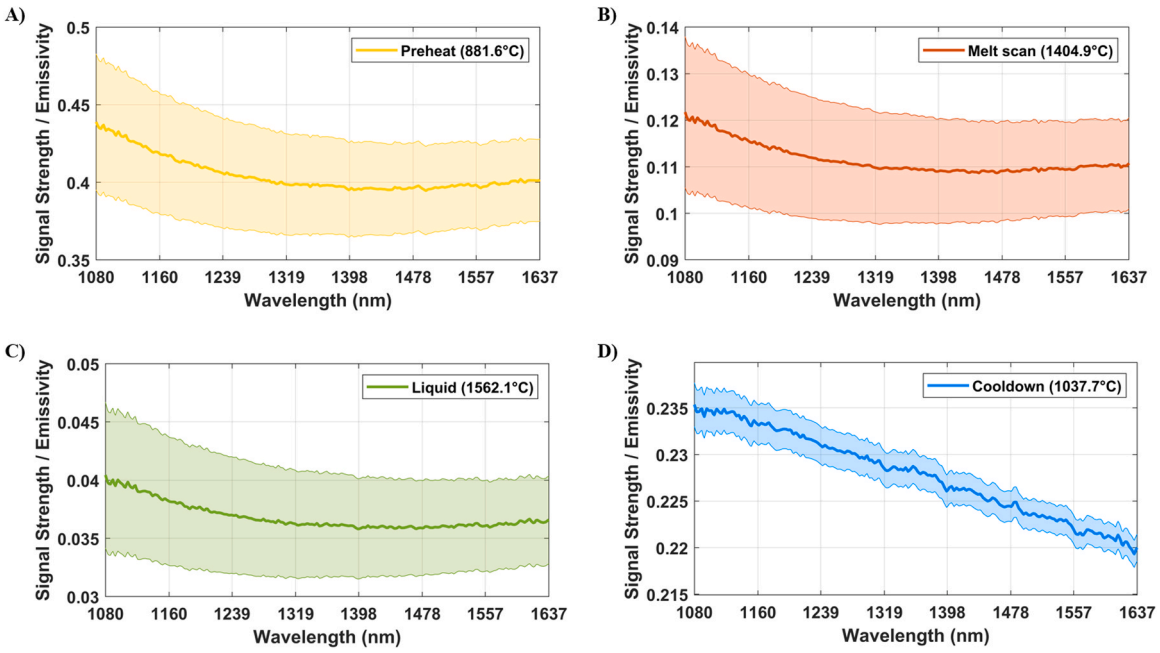

Fig. 9. Spectral distributions for Ti6Al4V shown for a single data point (median temperature measured) in A) Preheating, B) Melt scan, C) Liquid, and D) Cooldown process stages. The central line is the spectral data measured by the MW pyrometer whereas the bands represent the calculated uncertainty bounds.

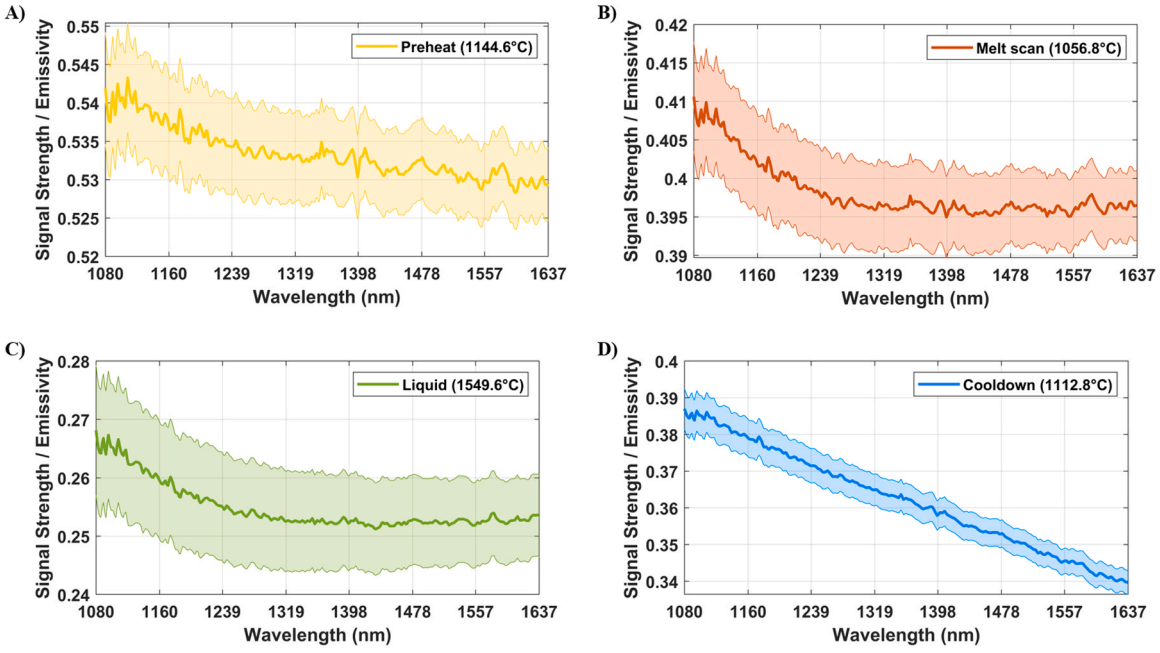

Fig. 10. Spectral distributions for TiAl shown for a single data point (median temperature measured) in A) Preheating, B) Melt scan, C) Liquid, and D) Cooldown process stages. The central line is the spectral data measured by the MW pyrometer whereas the bands represent the calculated uncertainty bounds.

correction for thermographic observations in PBF-EB considering discrete values of emissivity for the solid and liquid, but still constant [12]. An emissivity ($\varepsilon = 0.5$) dependent IR thermography technique for monitoring of the PBF-LB was presented in [57]. IR thermographs of the PBF-EB process were calibrated with constant emissivity values for sintered powder ($\varepsilon = 0.50$) and for solidified surfaces of Ti6Al4V ($\varepsilon = 0.26$) by Rodriguez *et. al* [8]. The work of [11] presented a calibration of IR thermography for PBF-EB using Inconel 718 but pointed out the lack of emissivity in the liquid stage as a source of error in observations. Outside the realm of PBF AM, Taminger *et. al.* used constant values of emissivity for Inconel 718 ($\varepsilon = 0.66$) and IN625 ($\varepsilon = 0.77$) for observations of the electron beam free form fabrication (EBF3) process.

To illustrate the potential errors that can be incurred by using the graybody assumption in PBF AM, an analysis was conducted employing equations, as defined in [6], to calculate the apparent temperature for a narrow band brightness pyrometer (Eq. 4), and for a ratio pyrometer (Eq. 5) where C_2 is the second radiation constant, and T is taken as the absolute temperature of a target.

$$T_{al} = \frac{C_2 T}{C_2 - \lambda_1 T \ln \varepsilon_1} \tag{4}$$

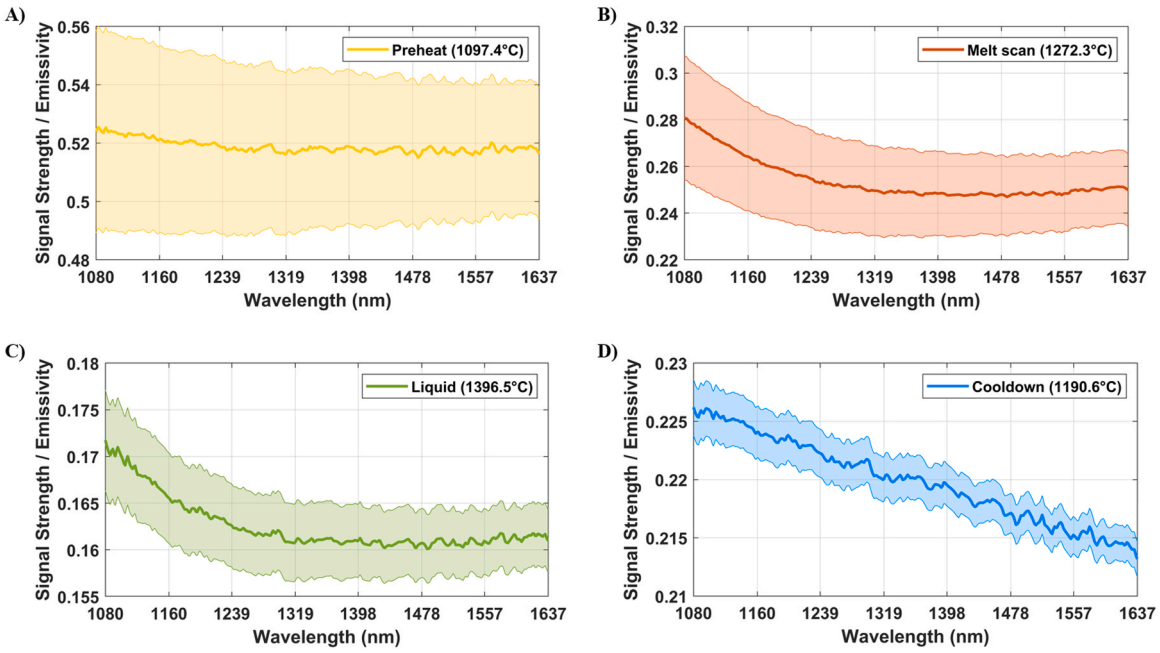

Fig. 11. Spectral distributions for 316 L shown for a single data point (median temperature measured) in A) Preheating, B) Melt scan, C) Liquid, and D) Cooldown process stages. The central line is the spectral data measured by the MW pyrometer whereas the bands represent the calculated uncertainty bounds.

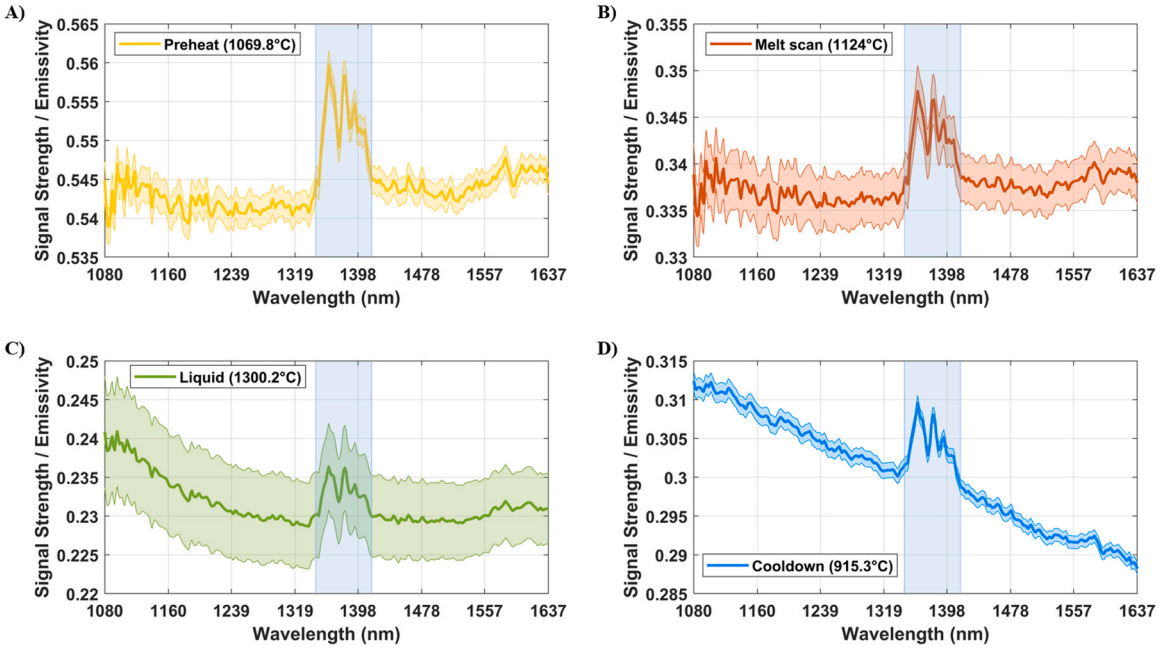

Fig. 12. Spectral distributions for IN625 shown for a single data point (median temperature measured) in A) Preheating, B) Melt scan, C) Liquid, and D) Cooldown process stages. The central line is the spectral data measured by the MW pyrometer whereas the bands represent the calculated uncertainty bounds.

Table 6
Maximum temperature uncertainty (u_T) and corresponding maximum uncertainty in signal strength / emissivity (u_ε) calculated for median temperatures occurring in the preheating, melt scanning, liquid, and cooldown process stages for each material.

Material	Preheating			Melt scanning			Liquid			Cooldown		
	T (°C)	u_T (°C)	u_ε	T (°C)	u_T (°C)	u_ε	T (°C)	u_T (°C)	u_ε	T (°C)	u_T (°C)	u_ε
Ti6Al4V	881.6	9.99	0.0438	1404.9	28.17	0.0162	1562.1	39.20	0.0063	1037.7	1.29	0.0024
TiAl	1144.6	2.04	0.0073	1056.8	2.48	0.0071	1549.6	11.33	0.0112	1112.8	2.08	0.0056
316 L	1097.4	9.31	0.0346	1272.3	20.16	0.0267	1396.5	6.58	0.0054	1190.6	1.71	0.0024
IN625	1069.8	0.56	0.0023	1124	1.56	0.0033	1300.2	5.57	0.0072	915.3	0.43	0.0013

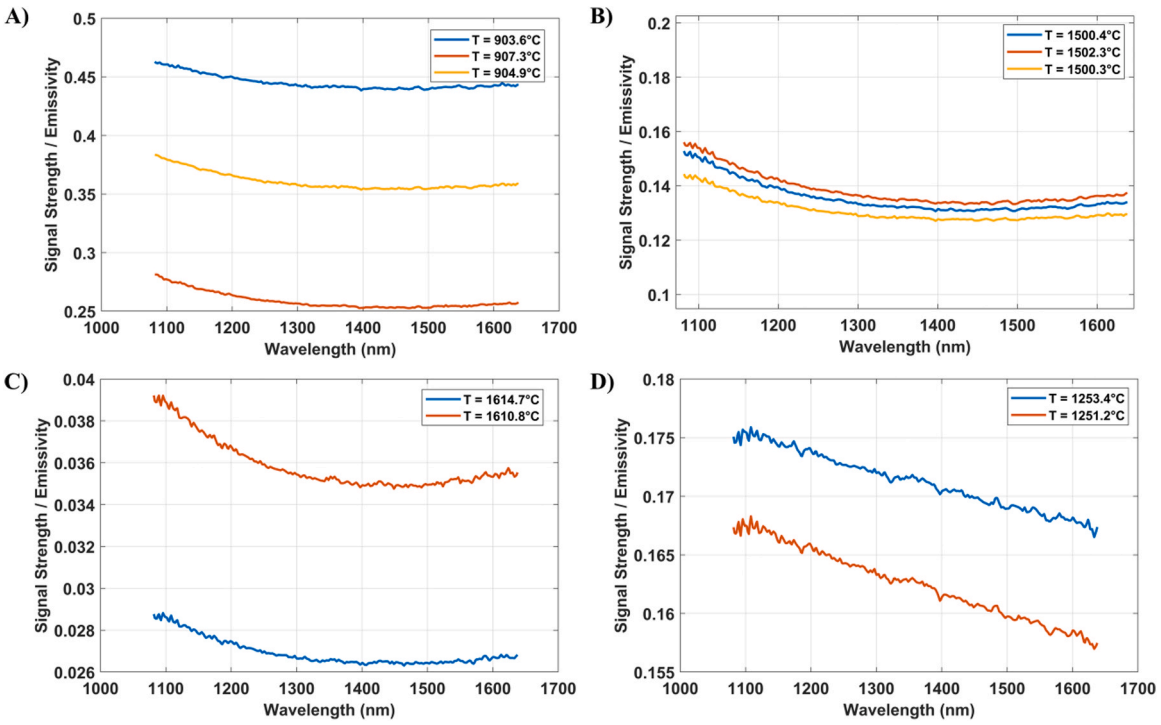

Fig. 13. Spectral variation of signal strength / emissivity of Ti6Al4V for three independent scans within + /- 5 °C of selected temperatures at A) preheat (905 °C), B) melt scan (1500 °C), liquid (1615 °C), and D) cooldown (1250 °C).

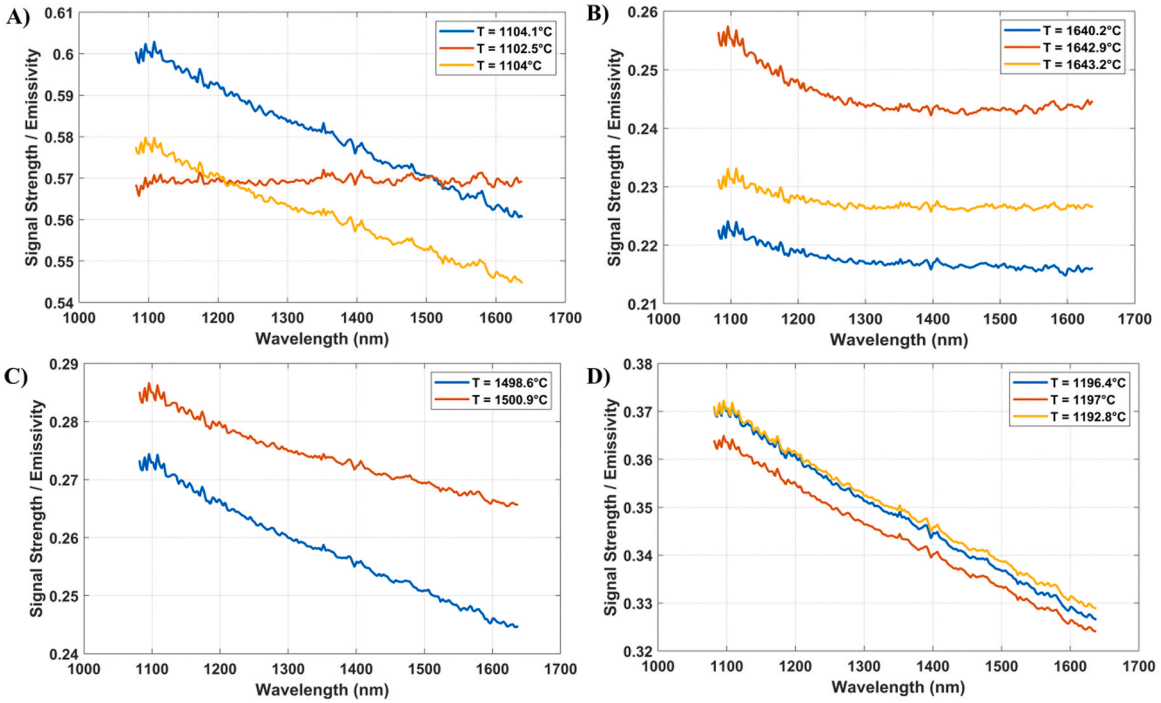

Fig. 14. Spectral variation of signal strength / emissivity of TiAl for three independent scans within + /- 5 °C of selected temperatures at A) preheat (1105 °C), B) melt scan (1645 °C), liquid (1500 °C), and D) cooldown (1195 °C).

$$\frac{1}{T_{ar}} = \frac{1}{T} + \frac{\lambda_2\lambda_1}{C_2(\lambda_2 - \lambda_1)} * \ln(\varepsilon_2/\varepsilon_1) \quad (5)$$

Eq. 4 was used to compute the apparent temperature (T_{al}) for several IR thermal imaging sensors reported in literature including sCMOS [12], MWIR using InSb detector [58], microbolometers operating in the long-wave infrared (LWIR) [8], and InGaAs photodiodes operating in the near infrared (NIR) [59], without accounting for the transmittance efficiency variations over the sensors' wavebands, by defining T = 1301.5 °C (a temperature measured by the FMPI in the melt stage for 316 L), and a common assumption of ε = 0.5 as in [57]. The plot in Fig. 17 shows the calculation of the apparent temperature throughout the spectral range for each of these sensors. The plots show that

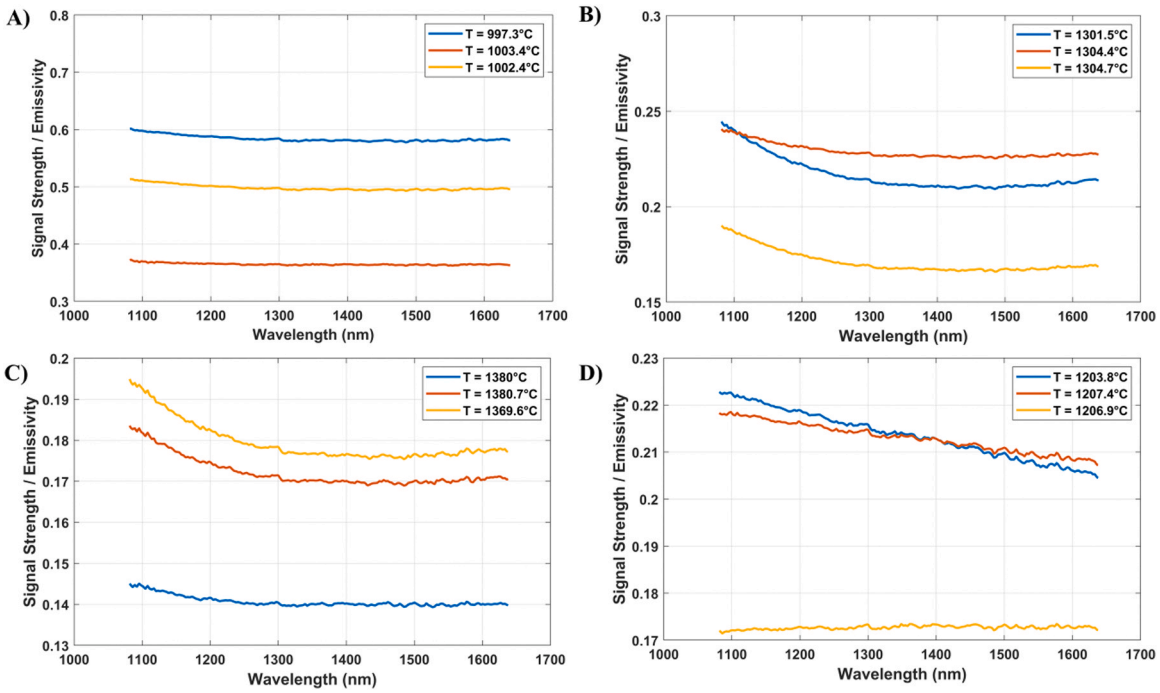

Fig. 15. Spectral variation of signal strength / emissivity of 316 L for three independent scans within + /- 5 °C of selected temperatures at A) preheat (1000 °C), B) melt scan (1300 °C), liquid (1375 °C), and D) cooldown (1205 °C).

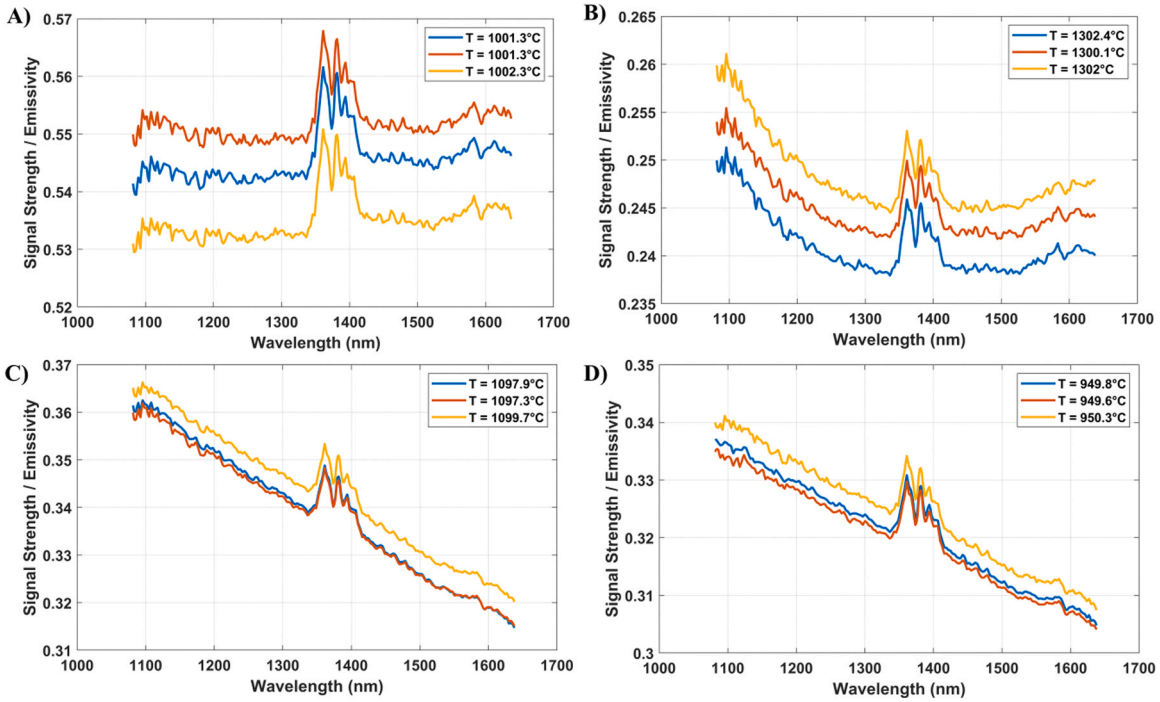

Fig. 16. Spectral variation of signal strength / emissivity of IN625 for three independent scans within + /- 5 °C of selected temperatures at A) preheat (1000 °C), B) melt scan (1300 °C), liquid (1095 °C), and D) cooldown (950 °C).

computed errors can range from tens of degrees for sCMOS and NIR sensors, while exceeding hundreds of degrees for other sensors. Specific values for the deviation in temperature (ΔT, °C) calculated at the central wavelength in the waveband for each sensor are annotated in Fig. 17 along with a computed percent difference from the actual, T = 1301.5 °C). Also, it is important to emphasize that, beyond these errors associated with the graybody assumption, these calculations ignore other sources of possible errors due to the optical path (stray reflections, window transmittance efficiency, absorption, or emission effects, etc.), which will only add to the potential measurement errors.

Using a similar approach, Eq. 5 was employed to compute the apparent temperature (T_{ar}) for ratio pyrometers described in literature with corresponding spectral channels centered at 750 nm and 900 nm for [18], 500 nm and 750 nm for [19], and photodiodes sensitive in the

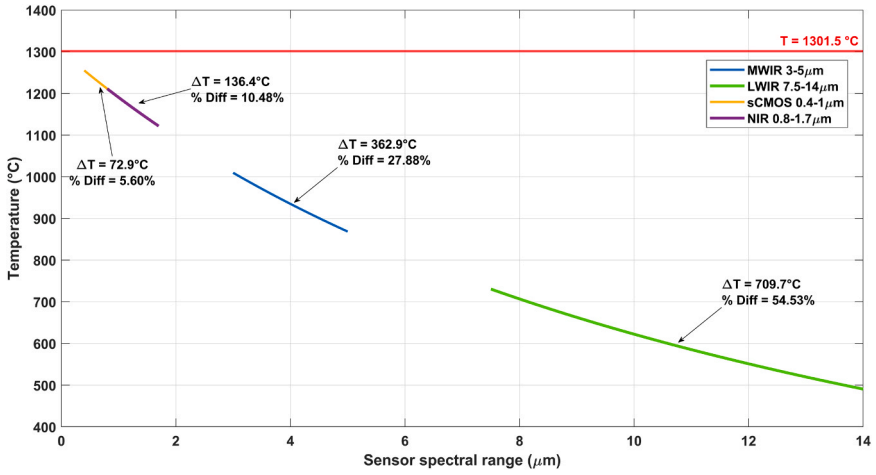

Fig. 17. Calculated apparent temperatures for several sensor technologies employed for IR imaging in PBF AM. Calculated temperatures disregard the efficiency of transmission on the spectral band.

bands of 1450–1650 nm and 1650–1800 nm [60]. For the analysis, the absolute temperature was again taken as T = 1301.5 °C. Under the graybody assumption through the spectrum, T_{ar} = T. However, using the spectral data for signal strength/emissivity for this measurement with max = 0.2456 and min = 0.2093 (Fig. 18), T_{ar} can vary as shown in Table 7.

The calculated apparent temperatures T_{ar} and deviation (ΔT) from a true temperature of T = 1301.5 °C are provided in Table 7 for the various ratio pyrometry setups reported in the AM literature [18,19,53]. For the specific spectral variation of emissivity shown in Fig. 18, the calculated values show errors ranging from tens of degrees (~3.6%) for the 500 nm/750 nm two-color to hundreds of degrees (~44.2% for the technique described in [53]). These calculations illustrate how the spectral nature of emissivity and the dynamic emissive behavior over time (transitions from gray to non-gray at different points in time while under similar thermal conditions) can impact the accuracy of the two-color measurement quite significantly.

With the foregoing analysis and discussion, it is expected that future works can benefit from the use of the data presented here to improve the accuracy of measurements and predictions. As a result, the raw data produced in this work is made available upon request to be used by the AM community, as necessary. Finally, although not the subject of this work, the data can be employed to approximate the absorptivity conditions occurring during fusion of the materials in PBF-LB (i.e., using emissivity at 1080 nm to approximate absorptivity near the laser wavelength, 1070 nm, typically used in PBF-LB). Laser absorptivity data can be used, for example, for the optimization of laser scanning strategies to improve laser scan track consistency, reduce undesired defects such as porosity from keyholing, among numerous other possibilities.

4. Conclusion

This work presented a MW pyrometry method adapted to perform in situ measurements of the transient spectral and temporal emissive behavior during PBF processing of four metal alloys in response to changes in temperature, phase, morphology, and chemistry. While studies in literature commonly report methods to obtain the emissivity of materials using potentially complicated setups with strict sample preparation methods, the approach used here enabled the near-continuous measurement of signal strength / emissivity during actual processing conditions experienced in PBF AM; the authors believe these measurements represent the first time the transient emissive behavior of materials being processed in PBF has been captured. Compared to other reported efforts, the measurements required no intricate preparation of the samples under study, thus providing a far more accurate representation of the conditions experienced by materials during the unfolding of the PBF process. The method presented can be adapted and applied for measurement during in process or in situ conditions for other metal fusion AM processes, including PBF-LB and directed energy deposition (DED).

The data presented here demonstrated the transitions in the thermal emissive behavior experienced by four alloys as these materials experienced phase changes from powder to liquid to solid. The approach involved an interplay of the settings for exposure time of the MW pyrometer, along with the use of specific PBF-EB process parameters to decrease the scan speed and effectively increase the amount of data captured in regions of interest that are highly transient (i.e., melt scanning and liquid). The plots presented for temperature and signal strength / emissivity versus time indeed revealed the effectiveness of this approach, since multiple repeatable melt events were captured with measured temperatures in agreement with the established melting ranges for each material.

Analysis of the data also revealed the drastic changes occurring to the

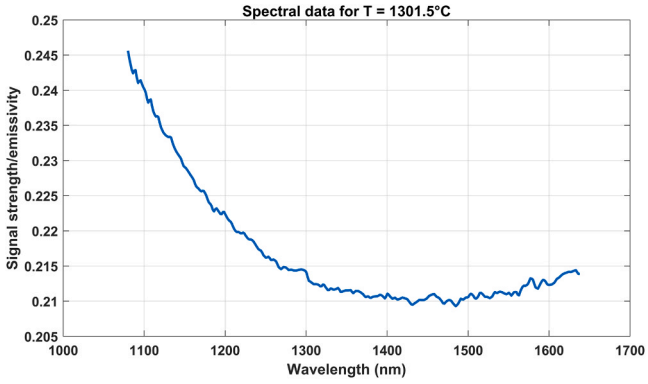

Fig. 18. Spectral signal strength/emissivity for a measured temperature of T = 1301.5 °C by the FMPI during melting of 316 L.

Table 7
Error in temperature (ΔT) and percent difference calculated for various ratio pyrometers assuming material to be gray.

Spectral Bands, [Reference]	T_{ar} (°C)	ΔT (°C)	% Difference
750 nm and 900 nm,[18]	1436.1	134.6	10.3%
500 nm and 750 nm,[19]	1343.9	42.4	3.6%
1450-1650 nm and 1650-1800 nm,[60]	1876.2	574.7	44.2%

signal strength / emissivity as the material experienced phase changes. Scatter plots of superimposed data for ten layers, with a common time datum, revealed the repeatable trends of the signal strength / emissivity in remarkable detail. The spectral behavior was shown in plots generated for selected data points corresponding to the median temperature observation in each process stage. In general, these plots showed a down trending spectral (i.e. wavelength dependent) emissive behavior indicating the non-grayness in various of the process stages defined, but mostclearly during cooldown.

Perhaps most significantly, the results indicated the variation in the spectral emissive behavior from scan to scan for each of the four alloys, including varying between gray and non-gray from scan to scan. The gray to non-gray variations from scan to scan are most exemplified for TiAl in Fig. 14 A) and 316 L in Fig. 15 D). It should further be noted that the MW pyrometry technique applied in this work successfully resolved the temperatures from scan to scan despite the varying gray and non-gray behavior of the material. These results suggest the extreme importance of using emissivity independent methods, such as the MW pyrometry method applied here, for measuring accurate processing temperatures while also highlighting the limitations of conventional radiation thermometry techniques when applied in PBF AM, specifically for brightness and ratio radiation thermometers as shown in the error analysis. The results computed for brightness and ratio devices demonstrate the potential error (hundreds of degrees or over 50% deviation for some devices) in the temperatures measured that can be incurred if a single emissivity is assumed, as is common practice when employing thermal radiation thermometry techniques. These errors are likely more severe when attempting measurements during the fast and transient conditions of PBF processing.

In summary, the results presented in this work detail the fast and dynamic variations in the thermal emissive behavior, including temporally varying gray and non-gray behavior from scan to scan, during materials processing in PBF AM. Contrasting with the current practice and belief that a priori knowledge of emissivity is adequate in PBF, the thermal emissive behavior of materials has been shown to be highly dynamic both temporally and spectrally during processing. As shown throughout our results, the measurements in signal strength / emissivity varied considerably during processing as a result of changes in temperature, morphology, chemistry, and phase. The use of emissivity independent in situ monitoring techniques, such as the one presented here, is deemed necessary to resolve accurate thermal signatures from in process conditions in PBF AM. It is hoped that the data presented here are helpful to the community when determining applicability of other emissivity dependent sensors (single or two-color pyrometers, including IR cameras), say, as an example, to employ commonly used radiation thermometry techniques when the emissive behavior is gray and well-behaved. Finally, these results and our future studies using this technique are intended to provide both improved physical understanding of emissive behavior of materials during processing as well as foundational data upon which improved numerical models can be developed.

Funding

Funding sources for this work are provided below: AFRL FA-8650–20-2-5700. LSAMP NSF HRD-1810898 (AF). Mr. and Mrs. MacIntosh Murchison Chair I in Engineering Endowment at UTEP (RW).

CRediT authorship contribution statement

Cesar A. Terrazas-Najera: Conceptualization, Experiment Design and Planning, Data Interpretation, Writing - review and editing, Writing - original draft, Analysis. **Alfonso Fernandez:** Experimental Design and Planning, Writing - original draft, Experimentation, Data acquisition. **Ralph Felice:** Data interpretation, Writing - review & editing. **Ryan Wicker:** Conceptualization, Supervision, Writing - review & editing, Funding acquisition, Project administration, Data interpretation.

Declaration of Competing Interest

One or more of the authors of this article are a part of the Editorial Board of the journal. To avoid a potential conflict of interest, the responsibility for the editorial and peer-review process of this article was with a different editor. Furthermore, the authors of this article were removed from the peer review process and had no, and will not have any, access to confidential information related to the editorial process of this article.

Data Availability

Data will be provided in formats enabling further analysis upon sensible request.

Acknowledgments

The work presented was performed at the W.M. Keck Center for 3D Innovation at the University of Texas at El Paso. The authors express gratitude to students Kurtis Watanabe, Alejandro Romero, and Emmanuel Levario for supporting this work by executing experiments and other aspects of the research.

Appendix A. – Uncertainty calculation

Uncertainty analysis.

Values of fractional uncertainty for each temperature measurement (u_T) were estimated and calculated using the quadrature sum as in Eq. A-1. The contributions to uncertainty were considered to include experimental uncertainties due to the temperature calculation, calibration of the device, and uncertainties due to a potentially non-uniform temperature within the target measurement region. More specifically, the uncertainty estimate (Eq. A-1) accounted for the tolerance as reported by the FMPI (u_{tol}), a fixed value for the uncertainty due to calibration (u_{cal}) that considered the calibration against the blackbody as the main contribution, and a computed value for the uncertainty arising from measuring a multi-phase, non-isothermal target (u_{tar}).

$$u_T = \sqrt{u_{tol}{}^2 + u_{cal}{}^2 + u_{tar}{}^2} \tag{A-1}$$

In Eq. A-1, u_{tol} is the uncertainty reported by the FMPI for each observation, accounting for the spectral signal strength and for environmental emission and absorption effects, as detailed in [24]. Next, u_{cal} was taken as the value reported from the blackbody manufacturer, a relative uncertainty contribution of 0.01% which is 0.1 °C at the calibration temperature of 1000 °C. Finally, u_{tar} was calculated employing an analysis like that presented by Ruffino [31] to obtain a measure of the uncertainty for a non-isothermal surface. In our work, the transient, non-isothermal surface was considered as the target observed by the FMPI consisting of a region where powder, liquid, and solidified material coexist during the selective melting induced by the traveling electron beam, as represented in Fig. 2 B). The influence of such non-isothermal target on the computed signal strength has been detailed in our recent work [22]. With reference to the schematic in Fig. 2 B), the temperature values computed from the emission captured by the FMPI, and

the signal strength values derived from these, are subject to a fill factor of the spot size as would happen for a melt-pool generated by a traveling heat source; whereas temperatures are influenced by the brightest or highest intensity area (A2), the signal strength values are biased toward the less bright or lower intensity parts of the target (A1 and A3).

The calculation of u_{tar} was carried out using Eq. A-2, where Λ is the effective wavelength, and the values of R as the intensity ratio, and Φ are defined in Eqs. A-3 and A-4, as follows:

$$u_{tar} = \frac{C_2}{\Lambda} \left[\frac{1}{\ln R - 5\ln\left(\frac{\lambda_1}{\lambda_2}\right)} - \frac{1}{\ln R + \ln(1-\Phi) - 5\ln\left(\frac{\lambda_1}{\lambda_2}\right)} \right] \tag{A-2}$$

$$R = \left(\frac{\lambda_1}{\lambda_2}\right)^5 e^{C_2 \Big/ T\left(\frac{1}{\lambda_1}-\frac{1}{\lambda_2}\right)} = \left(\frac{\lambda_1}{\lambda_2}\right)^5 e^{C_2 \Big/ T\left(\frac{1}{\Lambda}\right)} \tag{A-3}$$

$$\Phi = \frac{\frac{\beta}{\alpha}\left[e^{C_2/\lambda_1}\left(\frac{1}{T_1}-\frac{1}{T_2}\right) - e^{C_2/\lambda_2}\left(\frac{1}{T_1}-\frac{1}{T_2}\right)\right]}{1+\frac{\beta}{\alpha}e^{C_2/\lambda_1}\left(\frac{1}{T_1}-\frac{1}{T_2}\right)} \tag{A-4}$$

Also, the analysis as detailed by Ruffino required two temperature values for Eq. A-4; T_1 represented the highest measured temperature of the heat shield enclosure inside the PBF-EB system during experimentation, measured at 380 °C (for IN625) and used as the worst-case scenario for all calculations, whereas T_2 corresponded to each temperature measurement done by the FMPI at which the uncertainty was computed. Monitoring of the heat shield temperatures was performed using type K thermocouples attached to two walls of the heat shield enclosure. The heat shield enclosure was considered as a blackbody radiator (i.e. assuming perfect reflection and emission [25]), to compute the maximum possible contribution from the reflective environment to the uncertainty. However, the use of a constant value for emissivity, less than unity for brushed stainless steel, will minimize even further this contribution and the overall uncertainty in the measurements.

Once computed, the uncertainty in the temperature u_T was directly related to the uncertainty in signal strength (u_ε) via Eq. A-5, obtained as the first derivative of Planck's distribution law as shown in [61]. Also, for Eq. A-5, T corresponded to a given temperature observation made by the FMPI (in Kelvin), C_2 was taken as the second radiation constant, and lambda values corresponded to the wavelength at which spectral data was considered, as captured in the corresponding data file by the FMPI, for that observation.

$$u_{\varepsilon(\lambda,T)} = \varepsilon \left| \frac{C_2/\lambda T}{e^{-C2/\lambda T} - 1} \right| \frac{u_T}{T} \tag{A-5}$$

The uncertainty calculation computed using Eq. A-5 is presented in Figs. 9 through 12. Values of temperature uncertainty (u_T) and its effect on the signal strength / emissivity error (u_ε) which is employed to calculate the uncertainty bounds (shaded areas) for each plot presented in parts B) - E) in Figs. 9 through 12 in the main text.

References

[1] Y. Hagedorn, F. Pastors, Process monitoring of laser beam melting, Laser Tech. J. 15 (2018) 54–57, https://doi.org/10.1002/latj.201800009.

[2] L. Fuchs, C. Eischer, In-process monitoring systems for metal additive manufacturing, 2018.

[3] T. Grünberger, R. Domröse, Optical in-process monitoring of direct metal laser sintering (DMLS), Laser Tech. J. 11 (2014) 40–42, https://doi.org/10.1002/latj.201400026.

[4] B.K. Foster, E.W. Reutzel, A.R. Nassar, B.T. Hall, S.W. Brown, C.J. Dickman, Optical, layerwise monitoring of powder bed fusion, in: Solid Freeform Fabrication Symposium - An Additive Manufacturing Conference, 2015: pp. 295–307.

[5] M. Grasso, B.M. Colosimo, Process defects and in situ monitoring methods in metal powder bed fusion: a review, Meas. Sci. Technol. 28 (2017) 44005, https://doi.org/10.1088/1361-6501/AA5C4F.

[6] D.P. DeWitt, G.D. Nutter, Theory and Practice of Radiation Thermometry, John Wiley & Sons, Inc., 1988.

[7] H. Krauss, C. Eschey, M.F. Zaeh, Thermography for Monitoring the Selective Laser Melting Process, in: Solid Freeform Fabrication Sympossium, 2012.

[8] E. Rodriguez, J. Mireles, C.A. Terrazas, D. Espalin, M.A. Perez, R.B. Wicker, Approximation of absolute surface temperature measurements of powder bed fusion additive manufacturing technology using in situ infrared thermography, Addit. Manuf. 5 (2015), https://doi.org/10.1016/j.addma.2014.12.001.

[9] J. Mireles, C. Terrazas, S.M. Gaytan, D.A. Roberson, R.B. Wicker, Closed-loop automatic feedback control in electron beam melting, Int. J. Adv. Manuf. Technol. 78 (2015) 1193–1199, https://doi.org/10.1007/s00170-014-6708-4.

[10] R.B. Dinwiddie, M.M. Kirka, P.D. Lloyd, R.R. Dehoff, L.E. Lowe, G.S. Marlow, Calibrating IR cameras for in-situ temperature measurement during the electron beam melt processing of Inconel 718 and Ti-Al6-V4, in: J.N. Zalameda, P. Bison (Eds.), 2016: p. 986107. https://doi.org/10.1117/12.2229070.

[11] J. Raplee, A. Plotkowski, M.M. Kirka, R. Dinwiddie, A. Okello, R.R. Dehoff, S. S. Babu, Thermographic microstructure monitoring in electron beam additive manufacturing, Sci. Rep. 7 (2017), https://doi.org/10.1038/srep43554.

[12] N. Boone, C. Zhu, C. Smith, I. Todd, J.R. Willmott, Thermal near infrared monitoring system for electron beam melting with emissivity tracking, Addit. Manuf. 22 (2018) 601–605, https://doi.org/10.1016/j.addma.2018.06.004.

[13] P.A. Hooper, Melt pool temperature and cooling rates in laser powder bed fusion, Addit. Manuf. 22 (2018) 548–559, https://doi.org/10.1016/J.ADDMA.2018.05.032.

[14] M. Yakout, I. Phillips, M.A. Elbestawi, Q. Fang, In-situ monitoring and detection of spatter agglomeration and delamination during laser-based powder bed fusion of Invar 36, Opt. Laser Technol. 136 (2021) 106741, https://doi.org/10.1016/j.optlastec.2020.106741.

[15] A.G. Demir, L. Mazzoleni, L. Caprio, M. Pacher, B. Previtali, Complementary use of pulsed and continuous wave emission modes to stabilize melt pool geometry in laser powder bed fusion, Opt. Laser Technol. 113 (2019) 15–26, https://doi.org/10.1016/j.optlastec.2018.12.005.

[16] G. Croset, G. Martin, C. Josserond, P. Lhuissier, J.J. Blandin, R. Dendievel, In-situ layerwise monitoring of electron beam powder bed fusion using near-infrared imaging, Addit. Manuf. 38 (2021) 101767, https://doi.org/10.1016/j.addma.2020.101767.

[17] J.B. Forien, N.P. Calta, P.J. DePond, G.M. Guss, T.T. Roehling, M.J. Matthews, Detecting keyhole pore defects and monitoring process signatures during laser powder bed fusion: a correlation between in situ pyrometry and ex situ X-ray radiography, Addit. Manuf. 35 (2020) 101336, https://doi.org/10.1016/j.addma.2020.101336.

[18] J.A. Mitchell, T.A. Ivanoff, D. Dagel, J.D. Madison, B. Jared, Linking pyrometry to porosity in additively manufactured metals, Addit. Manuf. 31 (2020) 100946, https://doi.org/10.1016/j.addma.2019.100946.

[19] C.K.P. Vallabh, X. Zhao, Melt pool temperature measurement and monitoring during laser powder bed fusion based additive manufacturing via single-camera two-wavelength imaging pyrometry (STWIP), J. Manuf. Process 79 (2022) 486–500, https://doi.org/10.1016/J.JMAPRO.2022.04.058.

[20] Y.S. Tolukian, D.P. DeWitt, Thermal Radiative Properties - Metallic Elements and alloys, in: THERMOPHYSICAL PROPERTIES OF MATTER, 1970.

[21] M. Vollmer, K.-Peter. Möllmann, Infrared Thermal Imaging Fundamentals, Research and Applications, Wiley-VCH Verlag GmbH & Co. KGaA, 2018. https://doi.org/10.1002/9783527693306.

[22] C.A. Terrazas-Nájera, A. Romero, R. Felice, R. Wicker, Multi-wavelength pyrometry as an in situ diagnostic tool in metal additive manufacturing: Detecting sintering and liquid phase transitions in electron beam powder bed fusion, Addit. Manuf. 63 (2023) 103404, https://doi.org/10.1016/J.ADDMA.2023.103404.

[23] R.A. Felice, Temperature Determining Device And Process, US 6,379,038 B1, 2002.

[24] R.A. Felice, Temperature Determining Device And Process, US 5,772,323, 1998.
[25] A. Fernandez, R. Felice, C.A. Terrazas, R. Wicker, Implications for accurate surface temperature monitoring in powder bed fusion: using multi-wavelength pyrometry to characterize spectral emissivity during processing, Addit. Manuf. (2021) 102138, https://doi.org/10.1016/j.addma.2021.102138.
[26] D.M. Olinger, R.A. Felice, J.V. Gray, Successful Pyrometry in Investment Casting, Investment Casting Institute 55th Technical Conference and Expo. (2007).
[27] R.A. Felice, D.A. Nash, Pyrometry of materials with changing, spectrally-dependent emissivity-Solid and liquid metals, AIP Conf. Proc. 1552 (8) (2013) 734–739, https://doi.org/10.1063/1.4819633.
[28] R.A. Felice, Expert System Spectropyrometer Results for Non-Black, Non-Grey, or Chaning Emissivity and Selectively Absorbing Environments, Electro-Techno-Exposition, Moscow. (2003). http://pyrometry.com/farassociates_moscowpaper.pdf.
[29] R.A. Felice, The Spectropyrometer – a Practical Multi-wavelength Pyrometer, in: 8th Symposium on Temperature: Its Measurement and Control in Science and Industry, 2002.
[30] R.A. Felice, Multispectral expert system spectropyrometer and its uses in industry and research, Thermosense XXVI 5405 (2004) 36, https://doi.org/10.1117/12.547800.
[31] G. Ruffino, Two-colour pyrometry on nonisothermal fields: a measurement problem in siderurgy, High. Temp. High. Press 6 (1974) 223–227.
[32] S.M. Gaytan, L.E. Murr, F. Medina, E. Martinez, M.I. Lopez, R.B. Wicker, Advanced metal powder based manufacturing of complex components by electron beam melting, Mater. Technol. 24 (2009) 180–190, https://doi.org/10.1179/106678509×12475882446133.
[33] C.A. Terrazas, J. Mireles, S.M. Gaytan, P.A. Morton, A. Hinojos, P. Frigola, R. B. Wicker, Fabrication and characterization of high-purity niobium using electron beam melting additive manufacturing technology, Int. J. Adv. Manuf. Technol. 84 (2015) 1115–1126, https://doi.org/10.1007/s00170-015-7767-x.
[34] M.A. Lodes, R. Guschlbauer, C. Körner, Process development for the manufacturing of 99.94% pure copper via selective electron beam melting, Mater. Lett. 143 (2015) 298–301, https://doi.org/10.1016/j.matlet.2014.12.105.
[35] A. Rai, M. Markl, C. Körner, A coupled Cellular Automaton–Lattice Boltzmann model for grain structure simulation during additive manufacturing, Comput. Mater. Sci. 124 (2016) 37–48, https://doi.org/10.1016/j.commatsci.2016.07.005.
[36] X. Gong, J. Lydon, K. Cooper, K. Chou, Beam speed effects on Ti-6Al-4V microstructures in electron beam additive manufacturing, J. Mater. Res 29 (2014) 1951–1959, https://doi.org/10.1557/JMR.2014.125/FIGURES/9.
[37] X. Wang, X. Gong, K. Chou, Scanning speed effect on mechanical properties of Ti-6Al-4V alloy processed by electron beam additive manufacturing, Procedia Manuf. 1 (2015) 287–295, https://doi.org/10.1016/J.PROMFG.2015.09.026.
[38] T. Scharowsky, V. Juechter, R.F. Singer, C. Körner, Influence of the scanning strategy on the microstructure and mechanical properties in selective electron beam melting of Ti-6Al-4V, Adv. Eng. Mater. 17 (2015) 1573–1578, https://doi.org/10.1002/adem.201400542.
[39] J.C. Schuster, M. Palm, Reassessment of the binary aluminum-titanium phase diagram, J. Phase Equilibria Diffus 27 (2006) 255–277, https://doi.org/10.1361/154770306×109809.
[40] C.S. Kim, Thermophysical properties of stainless steels, (1975). https://doi.org/10.2172/4152287.
[41] M. Galati, A. Snis, L. Iuliano, Experimental validation of a numerical thermal model of the EBM process for Ti6Al4V, Comput. Math. Appl. 78 (2019) 2417–2427, https://doi.org/10.1016/J.CAMWA.2018.07.020.
[42] M. Balat-Pichelin, J.L. Sans, E. Bêche, Spectral directional and total hemispherical emissivity of virgin and oxidized 316L stainless steel from 1000 to 1650 K, Infrared Phys. Technol. 123 (2022) 104156, https://doi.org/10.1016/J.INFRARED.2022.104156.
[43] M. Balat-Pichelin, J.L. Sans, E. Bêche, L. Charpentier, A. Ferrière, S. Chomette, Emissivity at high temperature of Ni-based superalloys for the design of solar receivers for future tower power plants, Sol. Energy Mater. Sol. Cells 227 (2021) 111066, https://doi.org/10.1016/J.SOLMAT.2021.111066.
[44] L. del Campo, R.B. Pérez-Sáez, L. González-Fernández, X. Esquisabel, I. Fernández, P. González-Martín, M.J. Tello, Emissivity measurements on aeronautical alloys, J. Alloy. Compd. 489 (2010) 482–487, https://doi.org/10.1016/j.jallcom.2009.09.091.
[45] L. González-Fernández, E. Risueño, R.B. Pérez-Sáez, M.J. Tello, Infrared normal spectral emissivity of Ti–6Al–4V alloy in the 500–1150 K temperature range, J. Alloy. Compd. 541 (2012) 144–149, https://doi.org/10.1016/J.JALLCOM.2012.06.117.
[46] R.A. Felice, Investment Casting Temperature Measurement, Foundry Management & Technology. (2006).
[47] Y.J. Liang, X. Cheng, H.M. Wang, A new microsegregation model for rapid solidification multicomponent alloys and its application to single-crystal nickel-base superalloys of laser rapid directional solidification, Acta Mater. 118 (2016) 17–27, https://doi.org/10.1016/J.ACTAMAT.2016.07.008.
[48] S. Thapliyal, P. Agrawal, P. Agrawal, S.S. Nene, R.S. Mishra, B.A. McWilliams, K. C. Cho, Segregation engineering of grain boundaries of a metastable Fe-Mn-Co-Cr-Si high entropy alloy with laser-powder bed fusion additive manufacturing, Acta Mater. 219 (2021) 117271, https://doi.org/10.1016/J.ACTAMAT.2021.117271.
[49] R. Cui, L. Wang, L. Yao, B. Li, Y. Su, L. Luo, R. Chen, J. Guo, H. Fu, On the solidification behaviors of AlCu5MnCdVA alloy in electron beam freeform fabrication: microstructural evolution, Cu segregation and cracking resistance, Addit. Manuf. 51 (2022) 102606, https://doi.org/10.1016/J.ADDMA.2022.102606.
[50] G. Zhang, J. Chen, M. Zheng, Z. Yan, X. Lu, X. Lin, W. Huang, Element vaporization of Ti-6Al-4V alloy during selective laser melting, Metals 2020 Vol. 10 (Page 435. 10) (2020) 435, https://doi.org/10.3390/MET10040435.
[51] K. Wei, Z. Wang, X. Zeng, Influence of element vaporization on formability, composition, microstructure, and mechanical performance of the selective laser melted Mg–Zn–Zr components, Mater. Lett. 156 (2015) 187–190, https://doi.org/10.1016/J.MATLET.2015.05.074.
[52] S.A. Khairallah, A.T. Anderson, A. Rubenchik, W.E. King, Laser powder-bed fusion additive manufacturing: physics of complex melt flow and formation mechanisms of pores, spatter, and denudation zones, Acta Mater. 108 (2016) 36–45, https://doi.org/10.1016/J.ACTAMAT.2016.02.014.
[53] G.L. Knapp, J. Coleman, M. Rolchigo, M. Stoyanov, A. Plotkowski, Calibrating uncertain parameters in melt pool simulations of additive manufacturing, Comput. Mater. Sci. 218 (2023) 111904, https://doi.org/10.1016/J.COMMATSCI.2022.111904.
[54] M.J. Li, J. Chen, Y. Lian, F. Xiong, D. Fang, An efficient and high-fidelity local multi-mesh finite volume method for heat transfer and fluid flow problems in metal additive manufacturing, Comput. Methods Appl. Mech. Eng. 404 (2023) 115828, https://doi.org/10.1016/J.CMA.2022.115828.
[55] X. Li, N. Polydorides, Fast heat transfer simulation for laser powder bed fusion, Comput. Methods Appl. Mech. Eng. 412 (2023) 116107, https://doi.org/10.1016/J.CMA.2023.116107.
[56] S. Waqar, Q. Sun, J. Liu, K. Guo, J. Sun, Numerical investigation of thermal behavior and melt pool morphology in multi-track multi-layer selective laser melting of the 316L steel, Int. J. Adv. Manuf. Technol. 112 (2021) 879–895, https://doi.org/10.1007/S00170-020-06360-0/FIGURES/15.
[57] B. Lane, S. Moylan, E.P. Whitenton, L. Ma, Thermographic measurements of the commercial laser powder bed fusion process at NIST, Rapid Prototyp. J. 22 (2016) 778, https://doi.org/10.1108/RPJ-11-2015-0161.
[58] F. Bayle, M. Doubenskaia, Selective laser melting process monitoring with high speed infra-red camera and pyrometer, Https://Doi.Org/10.1117/12.786940. 6985 (2008) 39–46. https://doi.org/10.1117/12.786940.
[59] R. Chen, M. Sodhi, M. Imani, M. Khanzadeh, A. Yadollahi, F. Imani, Brain-inspired computing for in-process melt pool characterization in additive manufacturing, CIRP J. Manuf. Sci. Technol. 41 (2023) 380–390, https://doi.org/10.1016/J.CIRPJ.2022.12.009.
[60] K. Gutknecht, M. Cloots, K. Wegener, Relevance of single channel signals for two-colour pyrometer process monitoring of laser powder bed fusion, Int. J. Mechatron. Manuf. Syst. 14 (2021) 111–127, https://doi.org/10.1504/IJMMS.2021.119152.
[61] H. Watanabe, J. Ishii, H. Wakabayashi, T. Kumano, L. Hanssen, Spectral Emissivity Measurements, in: Experimental Methods in the Physical Sciences, Academic Press, 2014: pp. 333–366. https://doi.org/10.1016/B978–0-12–386022-4.00009–1.